Water Enables Efficient CO$_2$ Capture from Natural Gas Flue Emissions in an Oxidation-Resistant Diamine-Appended Metal–Organic Framework

Rebecca L. Siegelman[#,†,⊥], **Phillip J. Milner**[#,†,⊥,◆], **Alexander C. Forse**[†,‡,§], **Jung-Hoon Lee**[∥,#], **Kristen A. Colwell**[§], **Jeffrey B. Neaton**[∥,#,▽], **Jeffrey A. Reimer**[§,⊥], **Simon C. Weston**[○], **Jeffrey R. Long**[*,†,§,⊥]

†Department of Chemistry, University of California, Berkeley, California 94720, United States

‡Berkeley Energy and Climate Institute, University of California, Berkeley, California 94720, United States

§Department of Chemical and Biomolecular Engineering, University of California, Berkeley, California 94720, United States

∥Department of Physics, University of California, Berkeley, California 94720, United States

⊥Materials Sciences Division, Lawrence Berkeley National Laboratory, Berkeley, California 94720, United States

#Molecular Foundry, Lawrence Berkeley National Laboratory, Berkeley, California 94720, United States

▽Kavli Energy Nanosciences Institute at Berkeley, Berkeley, California 94720, United States

○Corporate Strategic Research, ExxonMobil Research and Engineering Company, Annandale, New Jersey 08801, United States

[#] These authors contributed equally to this work.

Abstract

[*]Corresponding Author: jrlong@berkeley.edu.
[◆]Present Address: Department of Chemistry and Chemical Biology, Cornell University, Ithaca, New York, 14853, United States.

Supported by increasingly available reserves, natural gas is achieving greater adoption as a cleaner-burning alternative to coal in the power sector. As a result, carbon capture and sequestration from natural gas-fired power plants is an attractive strategy to mitigate global anthropogenic CO_2 emissions. However, the separation of CO_2 from other components in the flue streams of gas-fired power plants is particularly challenging due to the low CO_2 partial pressure (~40 mbar), which necessitates that candidate separation materials bind CO_2 strongly at low partial pressures (4 mbar) to capture 90% of the emitted CO_2. High partial pressures of O_2 (120 mbar) and water (80 mbar) in these flue streams have also presented significant barriers to the deployment of new technologies for CO_2 capture from gas-fired power plants. Here, we demonstrate that functionalization of the metal—organic framework $Mg_2(dobpdc)$ ($dobpdc^{4-}$ = 4,4′-dioxidobiphenyl-3,3′-dicarboxylate) with the cyclic diamine 2-(aminomethyl)piperidine (2-ampd) produces an adsorbent that is capable of 90% CO_2 capture from a humid natural gas flue emission stream, as confirmed by breakthrough measurements. This material captures CO_2 by a cooperative mechanism that enables access to a large CO_2 cycling capacity with a small temperature swing (2.4 mmol CO_2/g with T 100 °C). Significantly, multicomponent adsorption experiments, infrared spectroscopy, magic angle spinning solid-state NMR spectroscopy, and van der Waals-corrected density functional theory studies suggest that water enhances CO_2 capture in 2-ampd–$Mg_2(dobpdc)$ through hydrogen-bonding interactions with the carbamate groups of the ammonium carbamate chains formed upon CO_2 adsorption, thereby increasing the thermodynamic driving force for CO_2 binding. In light of the exceptional thermal and oxidative stability of 2-ampd–$Mg_2(dobpdc)$, its high CO_2 adsorption capacity, and its high CO_2 capture rate from a simulated natural gas flue emission stream, this material is one of the most promising adsorbents to date for this important separation.

Graphical Abstract
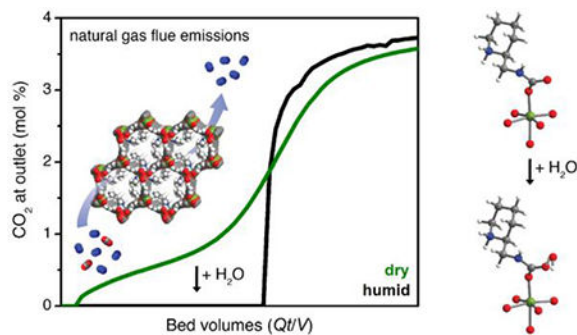
INTRODUCTION

The combustion of fossil fuels in the energy sector is currently responsible for the release of 32 Gt/year of CO_2 into the atmosphere, or approximately 65% of annual anthropogenic greenhouse gas emissions.[1,2] To limit the contribution of these emissions to global climate change, mitigation strategies are needed during the transition to cleaner fuel sources.[2] One of the most widely studied emission mitigation strategies is post-combustion carbon capture and sequestration (CCS), in which CO_2 is selectively removed from the flue gas streams of fossil fuel- or biomass-fired power plants and sequestered underground.[1–4] To date, the large

majority of efforts toward implementing CCS have focused on coal-fired power plants, which are currently responsible for approximately 45% of energy-related CO_2 emissions.[4,5] However, global consumption of natural gas has been increasing steadily, and its contribution to global primary energy is anticipated to overtake that of coal by 2040 (New Policy Scenario, International Energy Agency).[6] Furthermore, in economies where natural gas is prevalent, such as that of the United States, the rapid transition away from coal has resulted in CO_2 emissions from the combustion of natural gas already exceeding those from coal, despite the fact that natural gas emits approximately half as much CO_2 as coal per unit electricity produced.[7] Therefore, new materials are urgently needed for the selective removal of CO_2 from the emissions of natural gas-fired power plants.[8–10]

The flue gas stream produced at a natural gas combined cycle (NGCC) power plant consists of approximately 74.4% N_2, 12.4% O_2, 8.4% H_2O, 3.9% CO_2, and 0.9% Ar.[11] Importantly, emissions from NGCC plants contain fewer pollutants than emission streams from coal-fired plants, which release SO_x, NO_x, heavy metals, and particulate matter.[11] These contaminants pose environmental hazards and serve as significant barriers to the deployment of CCS systems in coal-fired plants, particularly due to the known poisoning of a number of CO_2 capture materials by SO_x and NO_x.[12–19] The CO_2 partial pressure of NGCC flue gas (~40 mbar) is also significantly lower than that of coal flue gas (~150 mbar).[11] As a result, gas-fired plants are cleaner-burning than coal-fired plants, but CO_2 capture from the emissions of these power stations is more technically challenging. Specifically, the U.S. Department of Energy (DoE) has set a target of 90% capture of CO_2 from the emission stream,[11] requiring that candidate CO_2 capture materials bind CO_2 at concentrations as low as 0.4%. Materials that meet this requirement often possess high CO_2 adsorption enthalpies,[20] necessitating energy-intensive cycling conditions and generating a potential tradeoff between heat management and CO_2 cycling capacity.[21]

Owing to decades of development, aqueous amine solutions are the most technology-ready systems for large-scale CO_2 capture applications.[22,23] However, amine solutions face technological barriers to deployment for CO_2 capture from NGCC power plants due to their high regeneration energy costs and susceptibility to oxidative and thermal degradation.[24–27] As an alternative, solid adsorbents, such as zeolites, amine-functionalized silicas, porous organic networks, and metal–organic frameworks, may offer enhanced stability, greater CO_2 cycling capacities, and inherently lower regeneration energies.[4,28–40] Despite the flourishing research areas of adsorptive CO_2 capture from coal flue gas and air, only a handful of reports have yet explored adsorbent design specifically for CCS from gas-fired power plants.[36,41–48] More research is also needed to design adsorbents with high thermal and oxidative stabilities that can capture CO_2 selectively under humid conditions.

Recently, we[49–53] and others[45,54–58] have demonstrated the potential of diamine-appended variants of the metal–organic framework Mg_2(dobpdc) (dobpdc^{4-} = 4,4′-dioxidobiphenyl-3,3′-dicarboxylate) as transformative materials for carbon capture applications.[59] The unique step-shaped adsorption profiles of these frameworks enable cycling of the full CO_2 adsorption capacity with minimal temperature swings. We have further shown that the adsorption step of these materials can be tuned post-synthetically by changing the appended diamine,[51] a strategy that we employed to optimize an adsorbent for

CO_2 capture from coal flue gas.[52] Our previous work posited that *primary,secondary* (1°/2°) diamine-appended variants of $Mg_2(dobpdc)$ are likely the most promising for CO_2 capture from NGCC flue gas, on the basis of their low CO_2 adsorption step pressures (<1 mbar at 40 °C) and minimal hysteresis upon CO_2 desorption.[51] However, these materials possess a tradeoff between thermal stability and CO_2 adsorption capacity. Specifically, the largest 1°/2° diamines were the most resistant to amine volatilization during temperature-swing cycling but also underwent a steric rearrangement at half saturation (0.5 CO_2 per diamine), which led to double-stepped CO_2 adsorption profiles.[53] As a result, at the low partial pressures relevant for NGCC CCS systems, only the capacity of the first CO_2 adsorption step (half of the theoretical capacity) would be accessible with such materials. While two similar base frameworks were shown to resolve the issue of steric crowding to enable single-step adsorption profiles with large diamines,[53] the initially studied $Mg_2(dobpdc)(diamine)_2$ variants remain preferable due to their inexpensive components and favorable gravimetric (~3.5–4.0 mmol/g) and volumetric (~79–84 v/v) CO_2 adsorption capacities.[51] Additionally, $Mg_2(dobpdc)$ has already been prepared at the multi-kilogram scale,[60] facilitating rapid technology development.

Herein, we demonstrate that appending the cyclic 1°/2° diamine 2-(aminomethyl)piperidine (2-ampd) to the metal sites in $Mg_2(dobpdc)$ alters the steric interactions and thermodynamics of CO_2 adsorption, giving rise to a material with two closely-spaced adsorption steps. The adsorbent 2-ampd–$Mg_2(dobpdc)$ (Figure 1) is thermally stable and exhibits two CO_2 adsorption steps at pressures low enough to access the full chemisorptive capacity of the material (1 CO_2 per diamine) from NGCC flue gas. Importantly, we find that the presence of water greatly improves the CO_2 adsorption characteristics of this material, enabling it to achieve 90% removal of CO_2 from simulated NGCC flue gas in breakthrough measurements. While other amine-functionalized adsorbents have shown improvements in CO_2 capture performance due to a humidity-induced mechanistic shift, our van der Waals (vdW)-corrected density functional theory (DFT) calculations and spectroscopy measurements show that the improved performance of 2-ampd–$Mg_2(dobpdc)$ under humid conditions can instead be attributed to preferential stabilization of the ammonium carbamate chains formed upon CO_2 insertion. Our results demonstrate that 2-ampd–$Mg_2(dobpdc)$ is among the most promising adsorbents identified to date for this underexplored but extremely important separation.

EXPERIMENTAL PROCEDURES

General Procedures.

^{1}H NMR spectra were collected on a Bruker AMX 300 MHz spectrometer and referenced to residual dimethyl sulfoxide (δ = 2.50 ppm). Powder X-ray diffraction (PXRD) patterns were collected with a laboratory Bruker AXS D8 Advance diffractometer with Cu Ka radiation (λ = 1.5418 Å) or at the Advanced Photon Source with synchrotron radiation (λ = 0.45399 Å), as specified in the figure captions. Additional details for synchrotron PXRD experiments under controlled atmospheres are given in Supporting Information Section 15. All synthetic manipulations were carried out under air unless noted otherwise. All solvents and reagents, including diamines, were purchased from commercial sources and used without further

purification unless otherwise noted. The linker H_4dobpdc was purchased from Hangzhou Trylead Chemical Technology Co. The linker H_4dotpdc was prepared according to the literature procedure.[53] The metal–organic frameworks Mg_2(dobpdc),[51] Mn_2(dobpdc),[52] Ni_2(dobpdc),[52] Co_2(dobpdc),[52] Zn_2(dobpdc),[61] and Mg_2(dotpdc)[53] were prepared according to literature procedures (Supporting Information Section 1). Ultrahigh purity (>99.998%) gases were used for all adsorption experiments.

Infrared Spectra.

Attenuated total reflectance (ATR) infrared (IR) spectra were collected on a PerkinElmer Spectrum 400 Fourier Transform (FT) IR spectrometer equipped with a Pike GladiATR and a home-built glovebag accessory used to control the atmosphere. Three vacuum–refill cycles were used to exchange the atmosphere of the glovebag accessory when preparing the system for *in situ* experiments. For humid FTIR spectra, samples were placed in 4 mL vials and sealed in a 20 mL vapor-dosing chamber containing ~4 mL of water. After at least 15 min of equilibration, the powder was removed, and spectra were collected. Co-adsorption of water in the sample was confirmed by observation of the H_2O IR vibrational bands at 1638 and 3350 (broad) cm^{-1}.[62]

Diamine Grafting Procedure.[51]

A 20 mL scintillation vial was charged with toluene (4 mL) and 2-ampd (1 mL). Methanol-solvated Mg_2(dobpdc) (~15 mg) was filtered and washed with toluene (2 × 10 mL). (Note: Mg_2(dobpdc) should not be allowed to dry completely in air due to potential decomposition.[49]) The filter-dried Mg_2(dobpdc) was added to the diamine solution, and the vial was swirled several times and allowed to stand at room temperature for at least 12 h. After this time, the mixture was filtered, and the resulting powder was washed with toluene (3 × 20 mL) and allowed to dry for ~3 min under reduced pressure, yielding ~25 mg of toluene-solvated 2-ampd–Mg_2(dobpdc). Other diamine-appended metal–organic frameworks described in this work were prepared using a similar procedure. Full characterization of all new diamine-appended frameworks prepared as part of this work, including PXRD patterns, IR spectra, dry N_2 thermogravimetric decomposition profiles, and CO_2 adsorption/desorption isobars, are included in the Supporting Information. Diamine loadings were determined by suspending ~5 mg of the diamine-appended metal–organic framework in 0.5 mL of DMSO-d_6 and then digesting the framework by adding several drops of DCl (35 wt % in D_2O) and heating until the mixture became homogeneous. The resulting solutions were analyzed by ^{1}H NMR spectroscopy to determine the ratio of diamine to organic linker. Representative diamine loadings for all diamine-appended metal—organic frameworks prepared as part of this work are included in the Supporting Information.

Thermogravimetric Analysis and Cycling Measurements.

Dry thermogravimetric analysis (TGA) experiments were conducted using a TA Instruments TGA Q5000. Humid TGA experiments were conducted using a TA Instruments TGA Q50. For humid experiments, the incident gas stream was passed through two room-temperature water bubblers in series, leading to an estimated water content of 2.6%, as determined by comparison to the water isotherms of 2-ampd–Mg_2(dobpdc) (Figure S11). Pre-mixed cylinders of CO_2 in N_2 were obtained from Praxair. Samples were activated under flowing

N$_2$ for 20–30 min until the mass stabilized; exact activation conditions for each diamine-appended material were determined through careful analysis of the dry N$_2$ thermal decomposition profiles and are included in the Supporting Information. Masses are uncorrected for buoyancy effects. A flow rate of 25 mL/min was used for all TGA experiments. Ramp rates for all isobaric measurements are included in figure captions. A ramp rate of 1.5 °C/min was employed for all dry N$_2$ decomposition experiments.

Gas Adsorption Measurements.

Volumetric adsorption isotherms for N$_2$, O$_2$, and CO$_2$ were obtained using a Micromeritics ASAP 2020 gas adsorption analyzer. Adsorption isotherms for water were obtained using a Micromeritics 3Flex instrument. For water isotherms, the stainless-steel vapor dosing apparatus was subjected to three freeze–pump–thaw cycles to remove any dissolved gases, and heat tape was used to keep the exposed portion of the glass sample tube at elevated temperature to prevent condensation of water. The maximum relative humidity accessible in measurements with water was limited by the manifold temperature of 45 °C. Isotherms collected at 40, 50, and 60 °C were measured using a circulating water bath to control the sample temperature. Surface area measurements with N$_2$ were carried out at 77 K using a liquid N$_2$ bath. Samples were regenerated at 100 °C under reduced pressure (<10 μbar) for 2–4 h between isotherms. The isotherm data points were considered equilibrated after <0.01% change in pressure occurred over an average of 11 intervals of 15 s (for N$_2$, O$_2$, and CO$_2$) or 30 s (for H$_2$O).

Calculation of Differential Enthalpies and Entropies of Adsorption.

Using a linear spline interpolation method and the CO$_2$ adsorption isotherms for 2-ampd–Mg$_2$(dobpdc) (Figure S7), the exact pressures (p_q) corresponding to specific CO$_2$ loadings (q) were determined at different temperatures (T). The Clausius–Clapeyron relationship (eq. 1) was used to calculate the differential enthalpies of adsorption (Δh_{ads}) based on the slopes of the linear trendlines fit to ln(p_q) vs. $1/T$ (Figure S8). The y-intercepts of these linear trendlines are equal to $-\Delta s_{ads}/R$ at each loading (assuming p_o = 1 bar)[63] and thus were used to determine the corresponding differential entropies of adsorption (Figure S9).

$$\ln\left(p_q\right) = \left(\frac{\Delta h_{ads}}{R}\right)\left(\frac{1}{T}\right) + c \qquad (1)$$

Breakthrough Measurements.

See Supporting Information Section 11 for experimental details and supplementary figures.

Solid-State Magic Angle Spinning (MAS) NMR Experiments.

Activation of 2-ampd–Mg$_2$(dobpdc) was carried out under flowing N$_2$ at 150 °C for 30 min. The activated material was packed into a 3.2 mm rotor inside a N$_2$-filled glovebag and further activated under vacuum inside a home-built gas manifold for 10 min at room temperature. This manifold has the key feature of enabling gas dosing of rotors at controlled pressures and subsequent sealing of dosed rotors prior to removal from the manifold.[61]

Samples were dosed with $^{13}CO_2$ gas (Sigma-Aldrich, 99 atom % ^{13}C, <3 atom % ^{18}O) at room temperature (~22 °C) and allowed to equilibrate for 30 min prior to measurements, unless otherwise specified. For dosing with humid CO_2, a sample that had already been dosed with dry $^{13}CO_2$ was opened (the top and bottom rotor caps were removed), and the sample was placed in a gas stream of humid CO_2 (relative humidity ~70%, measured using a ThermoPro TP50 Hygrometer) that was generated by flowing natural isotopic abundance CO_2 through a bubbler containing deionized water for 1 h.

All solid-state NMR experiments were carried out at 16.4 T using a Bruker 3.2 mm probe, and MAS rates were 15 kHz in all cases. All solid-state ^{13}C NMR spectra were acquired by cross-polarization from ^1H (^{15}N and ^1H contact RF field strengths of 20 kHz and 35 kHz, respectively). All cross-polarization experiments were acquired with continuous wave ^1H decoupling at 82 kHz RF field strength, and with the contact times stated in the figure captions. All ^1H NMR spectra were acquired using a 90° pulse-acquire sequence with a RF field strength of ~38 kHz, and recycle delays were adjusted to obtain quantitative spectra. The ^1H, ^{13}C, and ^{15}N chemical shifts were referenced to 1.8 ppm (adamantane), 38.5 ppm (adamantane tertiary carbon, left-hand resonance), and 33.4 ppm (glycine), respectively.[64]

Single-Crystal X-ray Diffraction.

Synthetic and experimental details for single-crystal X-ray diffraction experiments with 2-ampd–Zn_2(dobpdc) and molecular 2-ampd–CO_2 are included in Supporting Information Sections 12–14.

Density Functional Theory Calculations.

Our first-principles DFT calculations used a plane-wave basis and projector augmented-wave (PAW)[65,66] pseudopotentials with the Vienna ab-initio Simulation Package (VASP)[67–70] code. To include the effect of the vdW dispersive interactions on binding energies and NMR chemical shifts, we performed structural relaxations with vdW dispersion-corrected functionals (vdW-DF2)[71] as implemented in VASP. For all calculations, we used (i) a Γ-point sampling of the Brillouin zone (except for NMR calculations, as specified below), (ii) a 1000 eV plane-wave cutoff energy, and (iii) a 10^{-7} eV self-consistency criterion. We explicitly treat two valence electrons for Mg ($3s^2$), six for O ($2s^22p^4$), five for N ($2s^22p^3$), four for C ($2s^22p^2$), and one for H ($1s^1$). All structural relaxations were performed with a Gaussian smearing of 0.05 eV.[72] The ions were relaxed until the Hellmann-Feynman forces were less than 0.001 eVÅ^{-1}. To compute CO_2 and H_2O binding energies, we optimized the structure of 2-ampd–Mg_2(dobpdc) prior to CO_2 and H_2O adsorption ($E_{ampd–MOF}$), interacting with CO_2 and H_2O in the gas phase (E_{CO_2/H_2O}) within a 15 Å × 15 Å × 15 Å cubic supercell, and 2-ampd–Mg_2(dobpdc) with adsorbed CO_2 and H_2O molecules ($E_{CO_2-ampd–MOF}$) using vdW-corrected DFT. The binding energies (E_B) were obtained via the difference

$$E_B = E_{CO_2 - ampd - MOF} - \left(E_{ampd - MOF} + E_{CO_2/H_2O} \right) \qquad (2)$$

For NMR simulations, we used a $1 \times 1 \times 3$ k-point. With this k-point, the isotropic chemical shielding values (σ_{iso}) converged to 0.1 ppm. Since the isotropic chemical shift (δ_{iso}) is obtained from $\delta_{iso} = -(\sigma_{iso} - \sigma_{ref})$ where σ_{ref} is a reference value, we needed to determine a σ_{ref} value by comparing experimental δ_{iso} values to calculated σ_{iso} values. The σ_{ref} values for ^1H (31.4 ppm) and ^{13}C (160.1 ppm) were obtained by first computing σ_{iso} values for cocaine (CSD refcode COCAIN$_{10}$ was used as the starting point, and the structure was geometry optimized before NMR calculation; see Supporting Information for coordinates). The computed values were then compared with experimental values (Table S18, Figure S94).[73] The σ_{ref} value for ^{15}N (215.9 ppm) was determined by comparison of DFT-calculated σ_{iso} and the experimental δ_{iso} value for glycine (Table S18).[61] Additional DFT figures and details are included in Supporting Information Section 21.

RESULTS AND DISCUSSION

Adsorbent Design for NGCC Post-Combustion Capture.

Our previous crystallographic and gas adsorption studies of 1°,2° diamine-appended Mg$_2$(dobpdc) indicated that unfavorable chain-chain interactions in the *ab* plane of the framework give rise to the two-step adsorption profiles of these materials.[53] We reasoned that tethering the alkyl chain to the backbone of the diamine should alleviate these steric interactions, thereby minimizing the gap between the two CO$_2$ adsorption steps and enabling access to the full theoretical adsorption capacity. Accordingly, we grafted racemic 2-(aminomethyl)piperidine (2-ampd, Figure 1b) to Mg$_2$(dobpdc) using our previously reported procedure[51] to produce the adsorbent 2-ampd–Mg$_2$(dobpdc). Consistent with our hypothesis, this material exhibits two closely-spaced steps in its CO$_2$ adsorption isotherms (occurring at 1.0 and 3.7 mbar at 40 °C, respectively; see Figure 2). Importantly, both steps occur at pressures low enough to facilitate   90% removal of CO$_2$ (residual pressure of   4 mbar) from NGCC flue emissions under idealized, equilibrium conditions at 40 °C. In contrast, variants of Mg$_2$(dobpdc) functionalized with diamines bearing long alkyl substituents, such as *N*-(*n*-hexyl)ethylenediamine (*n*Hex-2),[53] have two widely spaced CO$_2$ adsorption steps, restricting the quantity of CO$_2$ that can be captured to the capacity of the lower-pressure step (~1.8 mmol/g at 40 mbar and 40 °C for *n*Hex-2, in contrast to 3.47 mmol/g for 2-ampd under the same conditions; Figure S16).

We hypothesize that step-shaped CO$_2$ adsorption in 2-ampd–Mg$_2$(dobpdc) arises as a result of cooperative insertion of CO$_2$ into the metal–amine bonds to form chains of ammonium carbamate running along the pore axis, as reported previously for related alkylethylenediamine-appended frameworks.[49–58] This conclusion is supported by spectroscopic characterization (discussed below) and by the observed metal dependence of the cooperative adsorption step position[50] for 2-ampd–M$_2$(dobpdc) variants (M = Mg, Mn, Ni, Co, Zn; Figure S85). In addition, appending 2-ampd within the expanded terphenyl framework Mg$_2$(dotpdc) (dotpdc^{4-} = 4,4″-dioxido-[1,1′:4′,1″-terphenyl]-3,3″-dicarboxylate) produces an adsorbent with only one step in its CO$_2$ adsorption isobar (Figure S21), confirming that the two adsorption steps observed for 2-ampd–Mg$_2$(dobpdc) also arise from steric interactions between adjacent diamines in the framework (Supporting Information Section 4). Importantly, 2-ampd–Mg$_2$(dobpdc) possesses comparable or

superior thermal stability to all other 1°/2° diamine-appended variants of $Mg_2(dobpdc)$ evaluated to date (Figure S6), withstanding 12 h of exposure to flowing, humid CO_2 at a regeneration temperature of 140 °C (or even as high as 180 °C) with minimal diamine volatilization (Table S15, see also discussion below). Therefore, the cyclic diamine 2-ampd uniquely affords the best attributes achieved with 1°/2° diamine-appended $Mg_2(dobpdc)$ materials to date, namely, high thermal stability coupled with a high CO_2 adsorption capacity from a NGCC flue gas stream.

The single crystal X-ray diffraction structure of the isostructural framework 2-ampd–$Zn_2(dobpdc)$ (Figure 1) provides insight into the thermal stability and close CO_2 adsorption steps of 2-ampd–$Mg_2(dobpdc)$. The bulky piperidine ring of 2-ampd can maintain a stable chair conformation in the pores of the framework, with efficient packing in the *ab* plane and minimization of unfavorable interactions between adjacent diamines. Consistently, despite the high density of amine groups within the pores, 2-ampd–$Mg_2(dobpdc)$ exhibits a high Brunauer–Emmett–Teller surface area of 618 ± 2 m^2/g (Figure S4), which should enable rapid diffusion of CO_2 through the channels of the framework, even after CO_2 adsorption.

Single-Component Adsorption Experiments.

Following validation of these initial design criteria, we investigated additional properties relevant to the application of 2-ampd–$Mg_2(dobpdc)$ in CO_2 capture from NGCC flue emissions. Isothermal adsorption profiles were collected at 40, 50, and 60 °C for CO_2 and at 40 °C for N_2 and O_2 (Figure 2). For CO_2, two adsorption steps were observed at all temperatures. Both adsorption steps occur below 40 mbar even at 60 °C and are predicted to be operative in this target pressure range up to approximately 69 °C (Figure S14). Importantly, because 2-ampd–$Mg_2(dobpdc)$ adsorbs minimal CO_2 at partial pressures beneath the first step pressure, processes with higher adsorption temperatures can be considered without sacrificing CO_2 adsorption capacity, as would be expected for a typical Langmuir-type adsorbent. Eliminating the need to adsorb at the lowest possible temperature can potentially reduce process costs through relaxed requirements for flue gas cooling,[74] minimization of water co-adsorption,[47] and/or enhanced tolerance to temperature rise in the adsorbent bed upon exothermic CO_2 adsorption.[21] In addition, despite demonstrating strong adsorption of CO_2 at low partial pressures, 2-ampd–$Mg_2(dobpdc)$ can be fully regenerated by heating to only 140 °C under a flow of dry or humid CO_2 at atmospheric pressure (Figure S37). Furthermore, at the partial pressures relevant to natural gas flue emissions, 2-ampd–$Mg_2(dobpdc)$ demonstrates excellent non-competitive CO_2/N_2 and CO_2/O_2 selectivities of 1320 and 694, respectively (Table S1), which are among the highest reported for a non-size-selective metal–organic framework.[31,35,75–78] Because N_2 and O_2 cannot participate in the CO_2-selective cooperative adsorption mechanism, these values are anticipated to be reflective of the multicomponent performance of the material.

The thermodynamics of CO_2 adsorption in 2-ampd–$Mg_2(dobpdc)$ were analyzed using the data in Figure 2. A spline interpolation method was used to calculate lines of constant loading for the set of CO_2 isotherms from 40 to 60 °C. Employing the Clausius–Clapeyron relationship yielded a differential enthalpy of adsorption (h_{ads}) of -73 ± 2 kJ/mol at a loading of 1 mmol/g (Figure S8), similar to that observed for other diamine-appended

variants of Mg_2(dobpdc)[50–52] and smaller in magnitude than the low-coverage enthalpies reported for silicas functionalized with primary or secondary amines.[79] From this adsorption enthalpy, we calculated a projected regeneration energy of 2.8 MJ/kg CO_2 for a temperature swing adsorption (TSA) process consisting of capture from a 40 mbar stream of CO_2 at 40 °C and desorption under 1 bar of CO_2 at 140 °C (see Supporting Information Section 3; note that only CO_2 was considered in this calculation). This value is over 30% lower than the regeneration energy projected for a polyamine-functionalized silica for a similar process (3.9 MJ/kg CO_2, see Supporting Information Section 3),[48] reflecting the advantage of cooperative adsorbents for CO_2 capture applications. Furthermore, with a higher adsorption temperature of 60 °C, an even lower projected regeneration energy of 2.7 MJ/kg CO_2 may be possible for 2-ampd–Mg_2(dobpdc) (considering only CO_2; see Table S2). Notably, the thermodynamics of adsorption for 2-ampd–Mg_2(dobpdc) were found to adhere to the same enthalpy–entropy correlation as other diamine-appended variants of Mg_2(dobpdc)[51] (Figure S15), corroborating the formation of ammonium carbamate chains upon CO_2 adsorption in this material.

Mixed-Gas Adsorption Experiments.

While single-component equilibrium data are needed to guide adsorbent design and characterize fundamental adsorption properties, multicomponent experiments are critical to evaluate adsorbent performance under more realistic process conditions. To that end, we performed extensive dry and humid thermogravimetric experiments with 2-ampd–Mg_2(dobpdc) using CO_2/N_2 mixtures and simulated NGCC flue emission streams. When exposed to a flow of dry simulated NGCC flue gas (4% CO_2 in N_2) at atmospheric pressure, 2-ampd–Mg_2(dobpdc) exhibits a high CO_2 capacity of 16.0 g/100 g (3.63 mmol/g) at 40 °C (Figure 3a, purple curve), consistent with the predicted capacity of 3.66 mmol/g for adsorption of 1 CO_2 per diamine. This adsorption capacity is significantly higher than that of other cyclic diamine-appended variants of Mg_2(dobpdc) (2.02–2.33 mmol/g, Figure S30), as well as the representative amine-functionalized silica MCM-41-PEI-50[80,81] (1.48 mmol/g, Figure S79) under equivalent conditions. However, for a dry 0.4% CO_2 in N_2 stream, representing the lowest adsorption pressure (4 mbar CO_2) required for 90% capture of CO_2 from NGCC emissions, the adsorption capacity at 40 °C (2.81 g/100 g, or 0.639 mmol/g, Figure 3a) is significantly lower than that observed in the 40 °C pure CO_2 isotherm at the same CO_2 partial pressure (2.76 mmol/g). Even with extremely slow isobaric cooling rates, similar discrepancies in the threshold conditions for cooperative adsorption have been observed between CO_2 adsorption isobars (collected under flowing CO_2/N_2 mixtures) and volumetric isotherms (collected under pure CO_2 starting from vacuum).[82,83] In general, the isobaric measurements show lower isobaric step temperatures (equivalent to higher isothermal step pressures) than would be expected given the measured equilibrium adsorption isotherms. These results suggest a smaller thermodynamic driving force for CO_2 capture under the more realistic, mixed-gas flow conditions. Additionally, we found that the adsorption capacity decreased when a faster cooling ramp rate (0.2 versus 0.1 °C/min) was employed, suggesting that the adsorption kinetics are limited in streams with low CO_2 partial pressures (Supporting Information Section 9). This result is consistent with a previous report investigating the adsorption kinetics of the related material mmen–Mg_2(dobpdc) (mmen = *N,N′*-dimethylethylenediamine).[84] Ultimately, thermodynamic and

kinetic factors under process-relevant flow conditions indicate that 2-ampd–Mg_2(dobpdc) falls short of achieving the target of 90% CO_2 capture from NGCC flue gas under *dry* conditions.

We also analyzed the ability of 2-ampd–Mg_2(dobpdc) to capture CO_2 in the presence of water, which can constitute up to ~8% of NGCC flue gas by volume. Humid isobars were collected by flowing CO_2/N_2 mixtures through two room-temperature water bubblers to generate an estimated water content of ~2.6 vol % (Figure 3b; see Figures S37–S46 and Tables S9 and S10 for direct comparisons of dry and humid isobars). Importantly, the temperature of each CO_2 adsorption step increased by 6 °C under humid conditions, with the step inflection points shifting from 111 to 117 °C and from 98 to 104 °C (solid green curves, Figure 3). These higher adsorption temperatures under humid conditions reflect thermodynamically more favorable cooperative adsorption of CO_2 in the presence of water. Likewise, under a flow of humid 4% CO_2 (40 mbar) in N_2, the inflection point of the higher-temperature adsorption step increased by ~14 °C, from 68 to 82 °C (purple curves, Figure 3). Critically, while 2-ampd–Mg_2(dobpdc) captures limited CO_2 from a dry stream containing 0.4% (4 mbar) CO_2 in N_2, the addition of humidity under the same conditions results in a sharp CO_2 step in the adsorption isobar, with an inflection point at 64 °C (orange curves, Figure 3). While the composition of the adsorbed phase cannot be determined directly from these experiments, a comparison of the humid CO_2/N_2 mixture isobars with a humid N_2 isobar indicates that the humid 0.4% CO_2 isobar involves the adsorption of CO_2 (orange and blue curves, Figure 3b). However, at lower temperatures, the saturation capacities of the humid CO_2/N_2 mixture isobars exceed the gravimetric uptake anticipated for adsorption of 1 CO_2 per diamine, suggesting co-adsorption of water. In sum, the isobaric adsorption data indicate that while 2-ampd–Mg_2(dobpdc) may fall below the target of 90% CO_2 capture from dry NGCC flue emissions, the presence of humidity in the gas stream should enable the material to reach this target at temperatures up to at least 60 °C.

To quantify the influence of water on the thermodynamics of CO_2 capture, approximate CO_2 adsorption enthalpies were calculated for the dry and humid CO_2/N_2 mixture isobars by employing the Clausius–Clapeyron relationship at the midpoint of each adsorption step. We note that while slow temperature ramp rates were used to approximate equilibrium conditions (Supporting Information Section 9), the enthalpies calculated from the adsorption isobars were found to be systematically higher than those calculated from the single-component, volumetric isotherms. Nonetheless, the difference between the humid and dry isobar enthalpies ($h_{ads,humid} - h_{ads,dry}$) should reflect the enthalpic benefit of CO_2 adsorption in the presence of water. Using this method, we attribute the increased temperature of the first adsorption step to a 31 ± 2 kJ/mol increase in the effective $-h_{ads}$ in the presence of water (dry: 81 ± 1 kJ/mol; humid: 112 ±2 kJ/mol). Notably, within error, the same increase in effective $-h_{ads}$ was found for the lower-temperature adsorption step (30 ± 2 kJ/mol), indicating that water uniformly increases the thermodynamic driving force for both adsorption steps (Tables S7 and S8). Interestingly, minimal change was observed in the isobaric desorption step temperatures following saturation with CO_2/H_2O under the tested humidity, resulting in calculation of equivalent enthalpies within error (dry: 101 ± 1 kJ/mol; humid: 99 ± 1 kJ/mol; difference: −2 ± 2 kJ/mol). While these results are complicated by the

lower relative humidities at the elevated desorption temperatures, the similar dry and humid CO_2 desorption step temperatures suggest that water desorbs before CO_2.

In order to quantify the influence of water on the performance of 2-ampd–Mg_2(dobpdc), we collected single-component water adsorption isotherms at 30, 40, 50, and 60 °C. For all temperatures, the isotherms show a plateau at a loading of 1 H_2O per diamine, followed by condensation at higher relative humidities (Figures S10 and S11). Using the same spline interpolation method as for CO_2, a differential adsorption enthalpy of −65 ± 2 kJ/mol was calculated at a loading of 1 mmol H_2O/g (Figure S12). Assuming co-adsorption and desorption cycling of 1 water molecule per diamine–Mg^{2+} site alongside cycled CO_2, the regeneration energy of 2-ampd–Mg_2(dobpdc) would increase by up to 1.5 MJ/kg CO_2 to a total of 4.3 MJ/kg CO_2 (Supporting Information Section 3). We note that these values are only approximations, as they do not account for potential differences in the adsorption enthalpy of water on the CO_2-inserted and diamine-bound phases (see DFT calculations below), the potential effect of higher relative humidity levels on adsorption or desorption, and the relative adsorption/desorption kinetics of CO_2 vs. H_2O in the ultimate cycling configuration. Nonetheless, 2-ampd–Mg_2(dobpdc) is still predicted to afford significant energy savings over competing amine-based technologies such as a PEI-functionalized silica, which requires a regeneration energy of 4.7 MJ/kg CO_2 under similar conditions (Supporting Information Section 3)[48] and is susceptible to degradative reaction pathways, such as urea formation (Figures S74–S77, discussed in greater detail below). Therefore, while these measurements indicate that the presence of water in the incident gas stream improves the thermodynamic driving force for CO_2 adsorption in 2-ampd–Mg_2(dobpdc), this improvement comes at the potential cost of an increase in the regeneration energy associated with the desorption of co-adsorbed water. The co-cycled water would then need to be condensed prior to compression and transport of the captured CO_2.

Fixed-Bed Adsorption Experiments.

To evaluate the performance of 2-ampd–Mg_2(dobpdc) in a fixed-bed adsorption process, we conducted breakthrough experiments under dry and humid simulated NGCC flue gas. These experiments are particularly important for materials with step-shaped isotherms, which often give rise to complex, multimodal breakthrough profiles. Such profiles were originally anticipated for diamine-appended frameworks by Mazzotti and coworkers in a comprehensive modeling study,[45] and a review of the underlying theory is included in Supporting Information Section 10. In short, the breakthrough profile can be predicted from an isotherm with one or more inflection points by applying "Golden's Rule," alternatively known as the rubber band rule or string rule.[45,85–87] When applying this rule, an operating curve for adsorption is constructed by stretching a hypothetical "rubber band" beneath the adsorption isotherm from the initial state (0% CO_2) to the feed state (4% CO_2). In concentration regimes bounded by individual points of contact with the rubber band, a compressive "shock" is anticipated in the breakthrough profile. In concentration regimes where the rubber band runs along the isotherm, a dispersive "wave" is expected. With a step-shaped isotherm, the result is often a "shock–wave–shock" profile: an initial "shock" is generated as CO_2 slips through the bed at concentrations beneath the step, followed by a "wave" corresponding to a small increase in CO_2 concentration during the onset of the

cooperative adsorption step, and finally a second "shock" at full breakthrough (see Figure S52). Intuitively, *the shock–wave–shock profile can be understood as a manifestation of the general inability of a cooperative adsorbent to capture CO_2 once the CO_2 partial pressure in the bed drops below the step pressure.* Accordingly, this behavior is the basis for our design criterion to achieve 90% capture of CO_2 through the selection of adsorbents with step pressures at <10% of the feed concentration.[51]

Breakthrough experiments were conducted with 0.73 g of semi-spherical pellets of 2-ampd–Mg_2(dobpdc) (350–700 μm) under 28 sccm of 4% CO_2 in N_2 at 1.1 bar (Figure 4; details of pellet preparation and characterization are given in Supporting Information Section 11). Considering the single-component CO_2 adsorption isotherms, a CO_2 "slip" (initial shock) of ~0.02 mol % was predicted under dry flue gas at 40 °C (obtained from Golden's Rule, see Figure S54), corresponding to a capture rate of 99.5% from a stream containing 4% CO_2 (calculated as (1–0.02/4)×100%). However, with dry simulated flue gas, approximately 0.6 mol % CO_2 slip was detected at the outlet, corresponding to a lower maximum capture rate of 86%. In addition, the CO_2 capacity at exhaustion (full breakthrough) was found to be 2.4 ± 0.2 mmol/g, which fell short of the capacity of 3.5 mmol/g predicted from the adsorption isotherm. The breakthrough profile and capacity were highly reproducible following activation of the material at 120 °C under flowing He (Figure S55). Reducing the flow rate to 14 sccm at 40 °C improved the capture rate (~0.4 mol % slip, or 90% capture rate) and sharpness of the breakthrough profile, reflecting a potential limitation in kinetics, but the breakthrough capacity at exhaustion remained unchanged (Figure S56). As anticipated from the isotherms and isobars, increasing the temperature to 60 °C increased the CO_2 slip, resulting in a measured capture rate of only 62% (Figure S57; predicted capture rate, 88%). The CO_2 breakthrough capacity at exhaustion was calculated as 2.2 ± 0.2 mmol/g, which again fell short of that predicted from the isotherm (3.2 mmol/g) but was consistent with that predicted from the CO_2 mixture isobars (2.2 mmol/g). Therefore, these results suggest that isobars collected by flowing dry CO_2 mixtures (Figure 3a) may reflect adsorbent performance in dry breakthrough measurements more accurately than single-component, volumetric isotherms (Figure 2). We anticipate that the greater utility of mixed-gas isobars versus single-component isotherms will apply generally in the evaluation of other carbon capture materials, particularly those with step-shaped adsorption isotherms.

To test the effect of CO_2 concentration on the elution profile, a breakthrough experiment was conducted under 14 sccm of 15% CO_2 in N_2 at 40 °C and atmospheric pressure, simulating coal flue gas (Figure S58). In this experiment, negligible slip was observed (>99% CO_2 capture), and the CO_2 capacity (3.1 ± 0.2 mmol/g) was consistent with that of the equilibrium isotherm (3.6 mmol/g), considering the 92% diamine loading of the pellets. Therefore, the deviations from equilibrium behavior observed in breakthrough experiments with lower CO_2 concentrations (Figure 4), particularly with respect to high CO_2 slip and resulting low CO_2 capture rate, can likely be attributed to limitations in kinetics. As a result, non-equilibrium effects may limit the performance of diamine-appended frameworks with *dry* CO_2 mixtures at low partial pressures, a hypothesis supported by a recent investigation of another diamine-appended framework for CO_2 capture from air.[84]

We also evaluated the breakthrough behavior of the material under humid flue gas mixtures containing ~2 vol % H_2O. Gratifyingly, consistent with the humid isobar measurements (Figure 3b), a dramatic enhancement in CO_2 capture performance was observed in breakthrough experiments with humid simulated NGCC flue gas following pre-saturation of the adsorbent bed with water (Figure 4b). In particular, humidification completely eliminated the initial CO_2 slip at 40 °C, resulting in a CO_2 capture rate of >99% and a desirable single, sharp CO_2 breakthrough front. The CO_2 exhaustion capacity calculated at full breakthrough (2.4 ± 0.2 mmol/g) was equivalent to that of the dry experiment, with a usable CO_2 capacity of 2.2 ± 0.1 mmol/g satisfying the DoE target of an average of 90% CO_2 capture. This striking improvement in performance is clearly visible in an overlay of the dry and humid CO_2 breakthrough profiles at 40 °C (Figure 4c). Breakthrough experiments at 60 °C revealed similarly dramatic improvements in performance upon addition of humidity (Figures S59–60), with an increase in capture rate from 62% to >99% (see Table S11 for a summary of capture rate results). The very high capture rate under humid conditions at 60 °C suggests that even higher adsorption temperatures could be used to achieve smaller temperature swings. In ongoing work, we are developing methods to predict the breakthrough performance as a function of both relative humidity and temperature. The promising performance of 2-ampd–Mg_2(dobpdc) in humid breakthrough experiments supports its utility as a next-generation adsorbent for post-combustion CO_2 capture from NGCC flue emissions.

Influence of Water on CO_2 Adsorption.

Due to the sensitivity of the adsorption threshold to the local environment in cooperative adsorbents, it is of interest to determine whether the presence of water changes the nature of the chemisorbed phase or merely enhances the thermodynamic favorability of the ammonium carbamate chain mechanism in diamine-appended metal–organic frameworks. Considering related materials, water is well known to improve the CO_2 adsorption capacity of amine-functionalized silicas.[30,42,88–99] This effect is generally ascribed to a mechanistic shift from ammonium carbamate formation (0.5 CO_2:amine) to bicarbonate or stabilized carbamic acid formation (1 CO_2 per amine),[12,89–91,95,96,99–108] although some studies have debated the formation of bicarbonates or carbonates.[109–112] Furthermore, these reports largely focus on the influence of water on the adsorption capacity, with minimal discussion of the influence of water on the thermodynamics of adsorption and the desorption temperature.[89,92,113,114] Notably, our related vdW-corrected DFT study of the framework mmen–Mg_2(dobpdc) demonstrated a stabilization of up to 41 kJ/mol for the CO_2-inserted phase in the presence of water.[115] This result suggests that water enhances, rather than changes, the ammonium carbamate chain adsorption mechanism, but to date no study has yet combined experimental and computational methods to characterize the effect of water on the CO_2 adsorption pathway, capacity, and breakthrough profile of a diamine-appended metal—organic framework. Accordingly, we employed IR and NMR spectroscopy and vdW-corrected DFT calculations to probe the behavior of 2-ampd–Mg_2(dobpdc) under dry and humid conditions.

We first collected IR spectra of 2-ampd–Mg_2(dobpdc) in the presence of dry N_2, dry CO_2, and humid CO_2 (Figure 5). Upon exposure to dry CO_2 at 22 °C and atmospheric pressure,

broad C(O)O⁻ (1648 cm⁻¹) and sharp C–N/N–C(O)O⁻ (1362 and 1342 cm⁻¹) vibrations were observed, consistent with the anticipated ammonium carbamate chain mechanism.[114] Similar new vibrations were observed at 1637 cm⁻¹ and 1340 cm⁻¹ in the IR spectrum of the molecular ammonium carbamate 2-ampd–CO_2 compared to the spectrum of free molecular 2-ampd (Figures S61–S63; crystallographic data provided as Supporting Information). We note that the reported C(O)O⁻ stretches are shifted to higher energies compared to those generally assigned to carbamates in amine-functionalized silicas (1500–1600 cm⁻¹),[114] which we attribute to the strong hydrogen bonding between the ammonium and carbamate units in these materials. The presence of two C–N/N–C(O)O⁻ stretches in the IR spectrum of CO_2-dosed 2-ampd–Mg_2(dobpdc) further suggests the formation of two distinct ammonium carbamate products upon CO_2 adsorption. The C–N/N–C(O)O⁻ vibrations persist in the presence of humid CO_2, consistent with preservation of a chemisorptive mechanism, while the C(O)O⁻ band is obscured by the H–O–H bend at 1630 cm⁻¹ arising from co-adsorbed water.[102]

Solid-state NMR spectra obtained under dry and humid conditions provided greater experimental detail for the effect of water on CO_2 adsorption in 2-ampd–Mg_2(dobpdc) (Figure 6). The ¹³C NMR spectrum of 2-ampd–Mg_2(dobpdc) dosed with 1025 mbar of ¹³CO_2 at room temperature shows two predominant overlapping resonances at 162 and 163 ppm, as well as a weak shoulder at a higher chemical shift (Figure 6a), all of which can be ascribed to chemisorbed CO_2 species. (See Figure S87 for the ¹³C spectrum of activated 2-ampd–Mg_2(dobpdc) prior to exposure to CO_2.) We hypothesize that the two main ¹³C resonances (Figure 6a) correspond to two conformations of ammonium carbamate chains,[61] consistent with the IR spectrum collected under dry CO_2 (Figure 5). Notably, our previous NMR characterization of diamines exhibiting double-step CO_2 adsorption profiles also revealed multiple resonances for chemisorbed CO_2, which likely arise due to spectroscopically distinct conformations of the sterically hindered ammonium carbamate chains.[61] The weak shoulder at higher frequencies (Figure 6a) may be associated with incomplete equilibration (see Figure S90).

To interpret these results, we carried out additional 2D and ¹⁵N NMR experiments. A ¹H–¹³C HETCOR experiment with a short contact time (100 μs) was performed to probe correlations with hydrogen atoms that are proximal to the chemisorbed carbon species (*i.e.* within a few Å; Figure S89). In the 2D experiment, the two ¹³C resonances each show a major ¹H correlation at ~5 ppm. We assign this feature to the N–H group of an ammonium carbamate species, while the ¹³C peaks are attributed to the carbamate carbon atoms of two distinct conformations of ammonium carbamate chains.[61,116] The observed single N–H correlation supports CO_2 insertion into metal–1° amine bonds to produce metal-bound carbamate species, with proton transfer to neighboring secondary amines to form charge-balancing ammonium groups. This reactivity is consistent with the previous crystallographic characterization of CO_2 insertion into Zn_2(dobpdc) functionalized with 1°/2° diamines.[51] Additionally, the ¹⁵N NMR spectrum of 2-ampd–Mg_2(dobpdc) dosed with 1025 mbar of ¹³CO_2 featured two peaks at 46 and 76 ppm, consistent with nitrogen atoms in ammonium and carbamate groups, respectively (Figure S86).[50,61]

After exposure of 2-ampd–Mg_2(dobpdc) to a flow of humid CO_2 (natural isotopic abundance) for 1 h, the main two ^{13}C resonances were retained, but smaller linewidths were observed (Figure 6a; see also Figure S90 for similar data obtained with a longer CO_2 exposure time). Therefore, in further agreement with the IR data, these NMR spectra demonstrate retention of the ammonium carbamate product in the presence of water and exclude a water-induced change in the CO_2 chemisorption mechanism. Co-adsorption of water was also confirmed by collection of ^1H NMR spectra before and after exposure to wet CO_2. The difference ^1H spectrum (Figure 6b) shows positive intensity that can be attributed to co-adsorbed water and reveals a narrow component at 4.6 ppm, as well as broad components at ~9 and ~3 ppm. The highly shifted (~9 ppm) water peak supports the formation of strong hydrogen bonds following exposure to water (Figure 6b). Additionally, the ^1H NMR spectra of 2-ampd–Mg_2(dobpdc) following exposure to dry or humid CO_2 (Figure 6b) show an increase in linewidth of the amine resonances compared to the NMR spectrum of activated 2-ampd–Mg_2(dobpdc) (Figure S88), consistent with a reduction of amine mobility following CO_2 insertion.

Due to the structural complexity of 2-ampd–Mg_2(dobpdc), the CO_2-inserted structure could not be solved directly from the X-ray diffraction pattern of the microcrystalline powder or from single crystals of the isostructural Zn framework under dry or humid conditions. We thus turned to vdW-corrected DFT calculations to predict the structure and energetics upon CO_2 adsorption, H_2O adsorption, and co-adsorption of CO_2 and H_2O in 2-ampd–Mg_2(dobpdc) (Figure 7). For simplicity, all calculations were carried out using the left-handed enantiomer of the diamine in the right-handed enantiomer of the framework. An adsorption energy of −70 kJ/mol was calculated for insertion of CO_2 to form ammonium carbamate chains in Mg_2(dobpdc)(2-ampd–CO_2)$_2$. This value is in good agreement with the experimentally determined CO_2 adsorption enthalpy of −72 ± 5 kJ/mol averaged over a loading of 0 to 1 CO_2 per diamine (Figure S8). In the calculated structure of Mg_2(dobpdc)(2-ampd)$_2$(H_2O)$_2$, adsorbed water was found to interact with 2-ampd by donating a hydrogen bond to the secondary amine (O⋯N distance of 2.924 Å). Close H_2O⋯H_2O contacts in the *ab* plane (O⋯O distance of 2.867 Å) suggest that additional stabilization is provided by hydrogen bonding between water molecules. In the absence of CO_2, an adsorption energy of −51 kJ/mol was calculated for H_2O. This value is consistent with the experimental H_2O adsorption enthalpy of −50 ± 2 kJ/mol at low loadings (0.2 mmol/g, or 0.05 mmol H_2O per diamine) but is slightly lower than the average experimental enthalpy of −65 ± 2 kJ/mol over a loading range of 0 to 1 mmol H_2O per diamine (Figure S12). In practice, while the structure shown here represents the lowest-energy H_2O binding mode discovered in our 0 K calculations, H_2O may sample other binding sites or geometries within the pore at room temperature. Overall, the adsorption energies corresponding to the calculated CO_2- and H_2O-adsorbed structures of 2-ampd–Mg_2(dobpdc) are in reasonable agreement with those determined from single-component adsorption measurements.

The DFT-calculated structure of Mg_2(dobpdc)(2-ampd–CO_2)$_2$(H_2O)$_2$ shows a strong hydrogen bonding interaction between H_2O and the metal-bound oxygen atom of the carbamate (O⋯O distance of 2.786 Å). Additionally, each H_2O molecule accepts a hydrogen bond from a carbamate nitrogen atom of the neighboring ammonium carbamate chain in the *ab* plane (N⋯O distance of 2.939 Å), resulting in a channel of H_2O molecules

between adjacent ammonium carbamate chains (Figure S95). A CO_2 adsorption energy of −88 kJ/mol was calculated for co-adsorption of 1 CO_2 and 1 H_2O per diamine, indicating that water increases the magnitude of the CO_2 binding energy by an estimated 18 kJ/mol compared to CO_2 insertion under dry conditions (binding energy of −70 kJ/mol). This value is smaller than the 31 ± 2 kJ/mol increase in − h_{ads} calculated from the humid vs. dry pure CO_2 adsorption isobars, but a comparison of the absolute values may be complicated by non-equilibrium effects in the isobars and the inability to determine the precise composition of the adsorbed phase. Notably, the DFT-calculated binding energy of CO_2 is larger than that of water in the co-adsorbed structure, suggesting that the endothermic penalty to desorb H_2O is smaller, and thus H_2O is likely to desorb first. This result is consistent with the minimal differences in the dry and humid CO_2 desorption temperatures observed in mixed-gas isobars (Figure 3). We note that the calculated and experimental NMR shifts for 2-ampd–Mg_2(dobpdc) exposed to dry and humid CO_2 also agree well with the experimental values (Table S20).

Taken together, the humid isobars, breakthrough measurements, spectroscopic data, and vdW-corrected DFT calculations support an increase in the favorability of CO_2 insertion under humid conditions, as a result of an enhancement of the ammonium carbamate chain formation mechanism in the presence of water. In humid breakthrough experiments, the resulting effective decrease in the isothermal CO_2 adsorption step pressure alters the propagation of the adsorption front through the bed. In particular, the single "shock" in the humid CO_2 breakthrough profile suggests that water reduces the effective step pressure and/or alters the shape of the CO_2 adsorption profile at low partial pressures, leading to more favorable performance under humid conditions (Figure S53).

Thermal, Oxidative, and Cycling Stability.

Beyond the thermodynamics and kinetics of adsorption, the long-term stability of an adsorbent is a critical consideration for ultimate industrial applications. In particular, the high oxygen content of the NGCC flue gas stream (~12%) is well known to lead to oxidative degradation of aqueous amine solutions.[24–27] To evaluate the oxidative stability of 2-ampd–Mg_2(dobpdc), the material was exposed to a flow of dry air (~21% O_2 in N_2) at 100 °C and atmospheric pressure for 5 h, and the dry, pure CO_2 isobars were compared before and after exposure. Minimal changes were observed in the CO_2 adsorption profile or capacity after this extensive O_2 treatment (Figure 8). In contrast, dry, oxygen-containing streams at 100 °C have been found to cause significant degradation of silicas functionalized with secondary amines.[117] In addition, no diamine oxidation products were detected by IR or by ^{1}H NMR spectroscopy after digestion of the O_2-treated material (Figure S72). The oxidative resistance of 2-ampd–Mg_2(dobpdc) is likely due in part to the fixed, wide spacing of diamines at metal sites ~7 Å apart along the channel direction, which serves to mitigate bimolecular (2 amine molecules) oxidation pathways observed in other materials.[117]

Adsorbents for carbon capture from NGCC flue gas must also withstand repeated thermal cycling under humid conditions. As part of this work, we found that the stability of diamine-appended variants of Mg_2(dobpdc) and related materials can be rapidly assessed by exposing the adsorbent to a flow of humid CO_2 for 12 h at the relevant desorption temperature (here,

140 °C) in a thermogravimetric analyzer, simulating hundreds of adsorption/desorption cycles (Supporting Information Section 16). The humid CO_2 adsorption capacities before and after such accelerated decomposition experiments can be compared in order to evaluate any capacity loss, and the material can be digested after the test to detect diamine volatilization or degradation. Notably, after treatment with flowing humid CO_2 at 140 °C for 12 h, 2-ampd–Mg_2(dobpdc) retains its step-shaped adsorption profile (Figure 8, blue curve) with only a slight capacity loss at 40 °C (original: 4.20 mmol/g; after humid CO_2 treatment: 4.11 mmol/g). In addition, almost no diamine volatilization (~2%) from the framework was observed. We further tested the stability of 2-ampd–Mg_2(dobpdc) to accelerated decomposition experiments at higher temperatures, representative of a potential process failure. At temperatures as high as 180 °C, 2-ampd–Mg_2(dobpdc) retains more than 90% of its adsorption capacity (Table S15), and the material remains highly crystalline even after treatment with a humid CO_2 stream at 220 °C for 12 h (Figure S70). Evaluation of a number of promising diamine-appended variants of Mg_2(dobpdc) for CO_2 capture from NGCC flue gas further revealed that the thermal stability of 2-ampd–Mg_2(dobpdc) is nearly unparalleled among this family of materials (Table S14). In addition, the stability of 2-ampd–Mg_2(dobpdc) is far superior to that of the representative amine-functionalized silica MCM-41-PEI-50, which undergoes urea formation and significant capacity loss (~17%) at 40 °C following exposure to humid CO_2 for 12 h at 140 °C (Figures S75–S77). The exceptional stability of 2-ampd–Mg_2(dobpdc) to humid gas streams at high temperatures makes it particularly promising for long-term application in a CO_2 capture process.

The stability of 2-ampd–Mg_2(dobpdc) in a TSA process was further evaluated by performing 750 adsorption (humid 4% CO_2 in N_2, 40 °C) and desorption (humid CO_2, 140 °C) cycles using a thermogravimetric analyzer (Figure 9, see Supporting Information Figure S80 for the full cycling data). Consistent with the accelerated decomposition test results (Figure 8), 2-ampd–Mg_2(dobpdc) exhibited a stable cycling capacity under humid simulated NGCC flue gas (Figure 9). The same final diamine loading (~94%) was observed after both 200 and 750 cycles, suggesting that the loading stabilizes after a small amount of initial diamine volatilization, likely from weakly-bound defect or surface sites. Notably, a high CO_2/H_2O cycling capacity of 16.0 g/100 g was observed for the 750th cycle, comparable to the adsorption capacity from a dry 4% CO_2 in N_2 stream at 40 °C (15.8 g/100 g). Nearly the same cycled capacity (15.3 g/100 g) could also be achieved over 200 tested cycles with a higher adsorption temperature of 60 °C (Figure S81). Short adsorption (5 min) and desorption (1 min) times were used in these experiments, indicating rapid kinetics despite the low CO_2 content of the simulated flue gas stream. Overall, the exceptional stability of 2-ampd–Mg_2(dobpdc) and excellent performance in breakthrough and cycling experiments support further development of this promising adsorbent for CO_2 capture from the emissions of gas-fired power plants.

CONCLUSIONS

Natural gas offers significant environmental advantages as an alternative to coal by enabling approximately 50% lower CO_2 emissions per unit of electricity produced. Capturing and sequestering the CO_2 emissions from gas-fired power plants provides an attractive option to achieve even greater emission reductions. We have shown that the metal–organic framework

2-ampd–Mg$_2$(dobpdc) is a promising candidate for post-combustion CO$_2$ capture from the emissions of NGCC power stations. In particular, as a result of the constituent cyclic diamine, this material overcomes the tradeoff between stability and capacity encountered with related cooperative adsorbents featuring linear 1°/2° diamines. Importantly, in breakthrough experiments simulating a fixed-bed adsorption process, 2-ampd–Mg$_2$(dobpdc) exhibits single-shock breakthrough profiles under humid conditions, in contrast to the multimodal elution profiles observed under dry conditions. This advantageous result is attributed to stabilizing H$_2$O–carbamate interactions, a conclusion supported by mixed-gas adsorption experiments, spectroscopic characterization, and vdW-corrected DFT calculations. Finally, 2-ampd–Mg$_2$(dobpdc) achieves the challenging practical criteria required of a material for CCS from NGCC emissions, namely a high CO$_2$ swing capacity as well as high thermal, oxidative, and cycling stability. Continued development of 2-ampd–Mg$_2$(dobpdc) at larger scales and in structured forms will enable modeling of heat and mass transfer and support bench-scale testing.

More broadly, this report achieves key advances toward the deployment of cooperative adsorbents in industrial CO$_2$ separations. First, we have reiterated the importance of considering CO$_2$ "slip" in adsorbent and process design for CO$_2$ capture applications with dry mixtures.[45,84] Second, and most importantly, we have established that pre-saturating the adsorbent bed with water can significantly enhance the CO$_2$ capture performance of diamine-appended, cooperative adsorbents by mitigating or eliminating CO$_2$ slip. Third, we have shown that experiments under flow conditions (such as isobars collected with slow temperature ramp rates under varying CO$_2$ concentrations) may predict the performance of cooperative adsorbents more accurately than single-component, volumetric adsorption isotherms. Finally, we have shown that TSA processes with cooperative adsorbents can utilize higher adsorption temperatures (here, 60 °C or higher instead of 40 °C) that could serve to mitigate water co-adsorption and reduce operating costs related to cooling the flue gas stream. Moving forward, we expect that these discoveries will be of value in the design of cooperative adsorbents for other challenging CO$_2$ capture processes, such as the direct capture of CO$_2$ from air.

Supplementary Material

Refer to Web version on PubMed Central for supplementary material.

ACKNOWLEDGMENTS

REFERENCES

(1). CO_2 Emissions from Fuel Combustion 2017 - Highlights; International Energy Agency: Paris, France, 2017.

(2). Pachauri RK; Allen MR; Barros VR; Broome J; Cramer W; Christ R; Church JA; Clarke L; Dahe Q; Dasgupta P Climate Change 2014: Synthesis Report. Contribution of Working Groups I, II and III to the Fifth Assessment Report of the Intergovernmental Panel on Climate Change; IPCC, 2014.

(3). Chu S Carbon Capture and Sequestration. Science 2009, 325 (5948), 1599–1599. 10.1126/science.1181637. [PubMed: 19779157]

(4). Bui M; Adjiman CS; Bardow A; Anthony EJ; Boston A; Brown S; Fennell PS; Fuss S; Galindo A; Hackett LA; Hallett JP; Herzog HJ; Jackson G; Kemper J; Krevor S; Maitland GC; Matuszewski M; Metcalfe IS; Petit C; Puxty G; Reimer J; Reiner DM; Rubin ES; Scott SA; Shah N; Smit B; Trusler JPM; Webley P; Wilcox J; Mac Dowell N Carbon Capture and Storage (CCS): The Way Forward. Energy Environ. Sci 2018, 11, 1062–1076. 10.1039/C7EE02342A.

(5). Stauffer PH; Keating GN; Middleton RS; Viswanathan HS; Berchtold KA; Singh RP; Pawar RJ; Mancino A Greening Coal: Breakthroughs and Challenges in Carbon Capture and Storage. Environ. Sci. Technol 2011, 45 (20), 8597–8604. 10.1021/es200510f. [PubMed: 21905694]

(6). World Energy Outlook 2017; International Energy Agency, 2017. 10.1787/weo-2017-en.

(7). Annual Energy Outlook 2018 with Projections to 2050; U.S. Energy Information Administration, 2018.

(8). CO_2 Capture at Gas Fired Power Plants; IEAGHG, 2012.

(9). Carbon Dioxide Capture for Natural Gas and Industrial Applications; Quadrennial Technology Review 2015; U.S. Department of Energy, 2015.

(10). Carbon Capture Opportunities for Natural Gas Fired Power Systems; U.S. Department of Energy, 2017.

(11). Cost and Performance Baseline for Fossil Energy Plants. Volume 1a: Bituminous Coal (PC) and Natural Gas to Electricity. Revision 3; DOE/NETL-2015/1723; U.S. Department of Energy, National Energy Technology Laboratory, 2015.

(12). Khatri RA; Chuang SSC; Soong Y; Gray M Thermal and Chemical Stability of Regenerable Solid Amine Sorbent for CO_2 Capture. Energy Fuels 2006, 20 (4), 1514–1520. 10.1021/ef050402y.

(13). Uyanga IJ; Idem RO Studies of SO_2- and O_2-Induced Degradation of Aqueous MEA during CO_2 Capture from Power Plant Flue Gas Streams. Ind. Eng. Chem. Res 2007, 46 (8), 2558–2566. 10.1021/ie0614024.

(14). Belmabkhout Y; Sayari A Isothermal versus Non-Isothermal Adsorption—Desorption Cycling of Triamine-Grafted Pore-Expanded MCM-41 Mesoporous Silica for CO_2 Capture from Flue Gas. Energy Fuels 2010, 24 (9), 5273–5280. 10.1021/ef100679e.

(15). Sjostrom S; Krutka H Evaluation of Solid Sorbents as a Retrofit Technology for CO_2 Capture. Fuel 2010, 89 (6), 1298–1306. 10.1016/j.fuel.2009.11.019.

(16). Han S; Huang Y; Watanabe T; Dai Y; Walton KS; Nair S; Sholl DS; Meredith JC High-Throughput Screening of Metal–Organic Frameworks for CO_2 Separation. ACS Comb. Sci 2012, 14 (4), 263–267. 10.1021/co3000192. [PubMed: 22432503]

(17). Yu K; Kiesling K; Schmidt JR Trace Flue Gas Contaminants Poison Coordinatively Unsaturated Metal–Organic Frameworks: Implications for CO_2 Adsorption and Separation. J. Phys. Chem. C 2012, 116 (38), 20480–20488. 10.1021/jp307894e.

(18). Hallenbeck AP; Kitchin JR Effects of O_2 and SO_2 on the Capture Capacity of a Primary-Amine Based Polymeric CO_2 Sorbent. Ind. Eng. Chem. Res 2013, 52 (31), 10788–10794. 10.1021/ie400582a.

(19). Rezaei F; Jones CW Stability of Supported Amine Adsorbents to SO_2 and NO_x in Postcombustion CO_2 Capture. 1. Single-Component Adsorption. Ind. Eng. Chem. Res 2013, 52 (34), 12192–12201. 10.1021/ie4019116.

(20). Berger AH; Bhown AS Selection of Optimal Solid Sorbents for CO_2 Capture Based on Gas Phase CO_2 Composition. Energy Procedia 2014, 63, 2092–2099. 10.1016/j.egypro.2014.11.225.

(21). Rezaei F; Grahn M Thermal Management of Structured Adsorbents in CO_2 Capture Processes. Ind. Eng. Chem. Res 2012, 51 (10), 4025–4034. 10.1021/ie201057p.

(22). Rochelle GT Amine Scrubbing for CO_2 Capture. Science 2009, 325 (5948), 1652–1654. 10.1126/science.1176731. [PubMed: 19779188]

(23). Bhown AS; Freeman BC Analysis and Status of Post-Combustion Carbon Dioxide Capture Technologies. Environ. Sci. Technol 2011, 45 (20), 8624–8632. 10.1021/es104291d. [PubMed: 21905745]

(24). Gouedard C; Picq D; Launay F; Carrette P-L Amine Degradation in CO_2 Capture. I. A Review. Int. J. Greenh. Gas Control 2012, 10, 244–270. 10.1016/j.ijggc.2012.06.015.

(25). Fredriksen SB; Jens K-J Oxidative Degradation of Aqueous Amine Solutions of MEA, AMP, MDEA, Pz: A Review. Energy Procedia 2013, 37, 1770–1777. 10.1016/j.egypro.2013.06.053.

(26). Vega F; Sanna A; Navarrete B; Maroto-Valer MM; Cortés VJ Degradation of Amine-based Solvents in CO_2 Capture Process by Chemical Absorption. Greenh. Gases Sci. Technol 2014, 4 (6), 707–733. 10.1002/ghg.1446.

(27). Mazari SA; Si Ali B; Jan BM; Saeed IM; Nizamuddin S An Overview of Solvent Management and Emissions of Amine-Based CO_2 Capture Technology. Int. J. Greenh. Gas Control 2015, 34, 129–140. 10.1016/j.ijggc.2014.12.017.

(28). Choi S; Drese JH; Jones CW Adsorbent Materials for Carbon Dioxide Capture from Large Anthropogenic Point Sources. ChemSusChem 2009, 2 (9), 796–854. 10.1002/cssc.200900036. [PubMed: 19731282]

(29). Bae Y-S; Snurr RQ Development and Evaluation of Porous Materials for Carbon Dioxide Separation and Capture. Angew. Chem. Int. Ed 2011, 50 (49), 11586–11596. 10.1002/anie.201101891.

(30). Bollini P; Didas SA; Jones CW Amine-Oxide Hybrid Materials for Acid Gas Separations. J. Mater. Chem 2011, 21 (39), 15100–15120. 10.1039/C1JM12522B.

(31). Li J-R; Ma Y; McCarthy MC; Sculley J; Yu J; Jeong H-K; Balbuena PB; Zhou H-C Carbon Dioxide Capture-Related Gas Adsorption and Separation in Metal-Organic Frameworks. Coord. Chem. Rev 2011, 255 (15–16), 1791–1823. 10.1016/j.ccr.2011.02.012.

(32). Wang Q; Luo J; Zhong Z; Borgna A CO_2 Capture by Solid Adsorbents and Their Applications: Current Status and New Trends. Energy Env. Sci 2011, 4 (1), 42–55. 10.1039/C0EE00064G.

(33). Liu J; Thallapally PK; McGrail BP; Brown DR; Liu J Progress in Adsorption-Based CO_2 Capture by Metal–Organic Frameworks. Chem Soc Rev 2012, 41 (6), 2308–2322. 10.1039/C1CS15221A. [PubMed: 22143077]

(34). Samanta A; Zhao A; Shimizu GKH; Sarkar P; Gupta R Post-Combustion CO_2 Capture Using Solid Sorbents: A Review. Ind. Eng. Chem. Res 2012, 51 (4), 1438–1463. 10.1021/ie200686q.

(35). Sumida K; Rogow DL; Mason JA; McDonald TM; Bloch ED; Herm ZR; Bae T-H; Long JR Carbon Dioxide Capture in Metal–Organic Frameworks. Chem. Rev 2012, 112 (2), 724–781. 10.1021/cr2003272. [PubMed: 22204561]

(36). Huck JM; Lin L-C; Berger AH; Shahrak MN; Martin RL; Bhown AS; Haranczyk M; Reuter K; Smit B Evaluating Different Classes of Porous Materials for Carbon Capture. Energy Environ. Sci 2014, 7 (12), 4132–4146. 10.1039/C4EE02636E.

(37). Webley PA Adsorption Technology for CO_2 Separation and Capture: A Perspective. Adsorption 2014, 20 (2–3), 225–231. 10.1007/s10450-014-9603-2.

(38). Lee S-Y; Park S-J A Review on Solid Adsorbents for Carbon Dioxide Capture. J. Ind. Eng. Chem 2015, 23, 1–11. 10.1016/j.jiec.2014.09.001.

(39). Sanz-Pérez ES; Murdock CR; Didas SA; Jones CW Direct Capture of CO_2 from Ambient Air. Chem. Rev 2016, 116 (19), 11840–11876. 10.1021/acs.chemrev.6b00173. [PubMed: 27560307]

(40). Ünveren EE; Monkul BÖ; Sarıoğlan Ş; Karademir N; Alper E Solid Amine Sorbents for CO_2 Capture by Chemical Adsorption: A Review. Petroleum 2017, 3 (1), 37–50. 10.1016/j.petlm.2016.11.001.

(41). Siegelman RL; Milner PJ; Kim EJ; Weston SC; Long JR Challenges and Opportunities for Adsorption-Based CO_2 Capture from Natural Gas Combined Cycle Emissions. Energy Environ. Sci 2019, 12 (7), 2161–2173. 10.1039/C9EE00505F. [PubMed: 33312228]

(42). Xu X; Song C; Miller BG; Scaroni AW Adsorption Separation of Carbon Dioxide from Flue Gas of Natural Gas-Fired Boiler by a Novel Nanoporous "Molecular Basket" Adsorbent. Fuel Process. Technol 2005, 86 (14), 1457–1472. 10.1016/j.fuproc.2005.01.002.

(43). Grande CA; Ribeiro RPPL; Rodrigues AE CO_2 Capture from NGCC Power Stations Using Electric Swing Adsorption (ESA). Energy Fuels 2009, 23 (5), 2797–2803. 10.1021/ef8010756.

(44). Seif El Nasr A; Nelson T; Kataria A; Abu-Zahra MRM Benchmarking of a Novel Solid Sorbent CO_2 Capture Process for NGCC Power Generation. Int. J. Greenh. Gas Control 2015, 42, 583–592. 10.1016/j.ijggc.2015.09.014.

(45). Hefti M; Joss L; Bjelobrk Z; Mazzotti M On the Potential of Phase-Change Adsorbents for CO_2 Capture by Temperature Swing Adsorption. Faraday Discuss. 2016, 192, 153–179. 10.1039/C6FD00040A. [PubMed: 27509258]

(46). Gibson JAA; Mangano E; Shiko E; Greenaway AG; Gromov AV; Lozinska MM; Friedrich D; Campbell EEB; Wright PA; Brandani S Adsorption Materials and Processes for Carbon Capture from Gas-Fired Power Plants: AMPGas. Ind. Eng. Chem. Res 2016, 55 (13), 3840–3851. 10.1021/acs.iecr.5b05015.

(47). Zhang W; Sun C; Snape CE; Irons R; Stebbing S; Alderson T; Fitzgerald D; Liu H Process Simulations of Post-Combustion CO_2 Capture for Coal and Natural Gas-Fired Power Plants Using a Polyethyleneimine/Silica Adsorbent. Int. J. Greenh. Gas Control 2017, 58, 276–289. 10.1016/j.ijggc.2016.12.003.

(48). Dijkstra JW; Walspurger S; Elzinga GD; Pieterse JAZ; Boon J; Haije WG Evaluation of Postcombustion CO_2 Capture by a Solid Sorbent with Process Modeling Using Experimental CO_2 and H_2O Adsorption Characteristics. Ind. Eng. Chem. Res 2018, 57 (4), 1245–1261. 10.1021/acs.iecr.7b03552.

(49). McDonald TM; Lee WR; Mason JA; Wiers BM; Hong CS; Long JR Capture of Carbon Dioxide from Air and Flue Gas in the Alkylamine-Appended Metal–Organic Framework mmen-Mg_2(dobpdc). J. Am. Chem. Soc 2012, 134 (16), 7056–7065. 10.1021/ja300034j. [PubMed: 22475173]

(50). McDonald TM; Mason JA; Kong X; Bloch ED; Gygi D; Dani A; Crocellà V; Giordanino F; Odoh SO; Drisdell WS; Vlaisavljevich B; Dzubak AL; Poloni R; Schnell SK; Planas N; Lee K; Pascal T; Wan LF; Prendergast D; Neaton JB; Smit B; Kortright JB; Gagliardi L; Bordiga S; Reimer JA; Long JR Cooperative Insertion of CO_2 in Diamine-Appended Metal-Organic Frameworks. Nature 2015, 519 (7543), 303–308. 10.1038/nature14327. [PubMed: 25762144]

(51). Siegelman RL; McDonald TM; Gonzalez MI; Martell JD; Milner PJ; Mason JA; Berger AH; Bhown AS; Long JR Controlling Cooperative CO_2 Adsorption in Diamine-Appended Mg_2(dobpdc) Metal–Organic Frameworks. J. Am. Chem. Soc 2017, 139 (30), 10526–10538. 10.1021/jacs.7b05858. [PubMed: 28669181]

(52). Milner PJ; Siegelman RL; Forse AC; Gonzalez MI; Runčevski T; Martell JD; Reimer JA; Long JR A Diaminopropane-Appended Metal–Organic Framework Enabling Efficient CO_2 Capture from Coal Flue Gas via a Mixed Adsorption Mechanism. J. Am. Chem. Soc 2017, 139 (38), 13541–13553. 10.1021/jacs.7b07612. [PubMed: 28906108]

(53). Milner PJ; Martell JD; Siegelman RL; Gygi D; Weston SC; Long JR Overcoming Double-Step CO_2 Adsorption and Minimizing Water Co-Adsorption in Bulky Diamine-Appended Variants of Mg_2(dobpdc). Chem. Sci 2018, 9 (1), 160–174. 10.1039/C7SC04266C. [PubMed: 29629084]

(54). Lee WR; Hwang SY; Ryu DW; Lim KS; Han SS; Moon D; Choi J; Hong CS Diamine-Functionalized Metal–Organic Framework: Exceptionally High CO_2 Capacities from Ambient Air and Flue Gas, Ultrafast CO_2 Uptake Rate, and Adsorption Mechanism. Energy Environ. Sci 2014, 7 (2), 744–751. 10.1039/C3EE42328J.

(55). Lee WR; Jo H; Yang L-M; Lee H; Ryu DW; Lim KS; Song JH; Min DY; Han SS; Seo JG; Park YK; Moon D; Hong CS Exceptional CO_2 Working Capacity in a Heterodiamine-Grafted Metal–

Organic Framework. Chem. Sci 2015, 6 (7), 3697–3705. 10.1039/C5SC01191D. [PubMed: 28706716]

(56). Jo H; Lee WR; Kim NW; Jung H; Lim KS; Kim JE; Kang DW; Lee H; Hiremath V; Seo JG; Jin H; Moon D; Han SS; Hong CS Fine-Tuning of the Carbon Dioxide Capture Capability of Diamine-Grafted Metal–Organic Framework Adsorbents Through Amine Functionalization. ChemSusChem 2017, 10 (3), 541–550. 10.1002/cssc.201601203. [PubMed: 28004886]

(57). Lee WR; Kim JE; Lee SJ; Kang M; Kang DW; Lee HY; Hiremath V; Seo JG; Jin H; Moon D; Cho M; Jung Y; Hong CS Diamine-Functionalization of a Metal–Organic Framework Adsorbent for Superb Carbon Dioxide Adsorption and Desorption Properties. ChemSusChem 2018, 11 (10), 1694–1707. 10.1002/cssc.201800363. [PubMed: 29603670]

(58). Kang M; Eun Kim J; Won Kang D; Young Lee H; Moon D; Seop Hong C A Diamine-Grafted Metal–Organic Framework with Outstanding CO_2 Capture Properties and a Facile Coating Approach for Imparting Exceptional Moisture Stability. J. Mater. Chem. A 2019, 7 (14), 8177–8183. 10.1039/C8TA07965J.

(59). Hong CS; Kang M; Kang DW Post-Synthetic Diamine-Functionalization of MOF-74 Type Frameworks for Effective Carbon Dioxide Separation. Dalton Trans. 2019, 48, 2263–2270. 10.1039/C8DT04339F. [PubMed: 30693920]

(60). Mosaic Materials, Inc http://mosaicmaterials.com/.

(61). Forse AC; Milner PJ; Lee J-H; Redfearn HN; Oktawiec J; Siegelman RL; Martell JD; Dinakar B; Porter-Zasada LB; Gonzalez MI; Neaton JB; Long JR; Reimer JA Elucidating CO_2 Chemisorption in Diamine-Appended Metal–Organic Frameworks. J. Am. Chem. Soc 2018, 140 (51), 18016–18031. 10.1021/jacs.8b10203. [PubMed: 30501180]

(62). NIST WebBook https://webbook.nist.gov/.

(63). Campbell CT; Sellers JRV Enthalpies and Entropies of Adsorption on Well-Defined Oxide Surfaces: Experimental Measurements. Chem. Rev 2013, 113 (6), 4106–4135. 10.1021/cr300329s. [PubMed: 23441680]

(64). Bertani P; Raya J; Bechinger B ^{15}N Chemical Shift Referencing in Solid State NMR. Solid State Nucl. Magn. Reson 2014, 61–62, 15–18. 10.1016/j.ssnmr.2014.03.003.

(65). Blöchl PE Projector Augmented-Wave Method. Phys. Rev. B 1994, 50 (24), 17953–17979. 10.1103/PhysRevB.50.17953.

(66). Kresse G; Joubert D From Ultrasoft Pseudopotentials to the Projector Augmented-Wave Method. Phys. Rev. B 1999, 59 (3), 1758–1775. 10.1103/PhysRevB.59.1758.

(67). Kresse G; Hafner J Ab Initio Molecular Dynamics for Liquid Metals. Phys. Rev. B 1993, 47 (1), 558–561. 10.1103/PhysRevB.47.558.

(68). Kresse G; Hafner J Ab Initio Molecular-Dynamics Simulation of the Liquid-Metal–Amorphous-Semiconductor Transition in Germanium. Phys. Rev. B 1994, 49 (20), 14251–14269. 10.1103/PhysRevB.49.14251.

(69). Kresse G; Furthmüller J Efficient Iterative Schemes for Ab Initio Total-Energy Calculations Using a Plane-Wave Basis Set. Phys. Rev. B 1996, 54 (16), 11169–11186. 10.1103/PhysRevB.54.11169.

(70). Kresse G; Furthmüller J Efficiency of Ab-Initio Total Energy Calculations for Metals and Semiconductors Using a Plane-Wave Basis Set. Comput. Mater. Sci 1996, 6 (1), 15–50. 10.1016/0927-0256(96)00008-0.

(71). Lee K; Murray ÉD; Kong L; Lundqvist BI; Langreth DC Higher-Accuracy van Der Waals Density Functional. Phys. Rev. B 2010, 82 (8), 081101. 10.1103/PhysRevB.82.081101.

(72). Elsässer C; Fähnle M; Chan CT; Ho KM Density-Functional Energies and Forces with Gaussian-Broadened Fractional Occupations. Phys. Rev. B 1994, 49 (19), 13975–13978. 10.1103/PhysRevB.49.13975.

(73). Baias M; Widdifield CM; Dumez J-N; Thompson HPG; Cooper TG; Salager E; Bassil S; Stein RS; Lesage A; Day GM; Emsley L Powder Crystallography of Pharmaceutical Materials by Combined Crystal Structure Prediction and Solid-State ^{1}H NMR Spectroscopy. Phys. Chem. Chem. Phys 2013, 15 (21), 8069–8080. 10.1039/C3CP41095A. [PubMed: 23503809]

(74). Ali U; Agbonghae EO; Hughes KJ; Ingham DB; Ma L; Pourkashanian M Techno-Economic Process Design of a Commercial-Scale Amine-Based CO_2 Capture System for Natural Gas

Combined Cycle Power Plant with Exhaust Gas Recirculation. Appl. Therm. Eng 2016, 103, 747–758. 10.1016/j.applthermaleng.2016.04.145.

(75). Zhang Z; Yao Z-Z; Xiang S; Chen B Perspective of Microporous Metal–Organic Frameworks for CO_2 Capture and Separation. Energy Environ. Sci 2014, 7 (9), 2868. 10.1039/C4EE00143E.

(76). Sabouni R; Kazemian H; Rohani S Carbon Dioxide Capturing Technologies: A Review Focusing on Metal Organic Framework Materials (MOFs). Environ. Sci. Pollut. Res 2014, 21 (8), 5427–5449. 10.1007/s11356-013-2406-2.

(77). Wang Q; Bai J; Lu Z; Pan Y; You X Finely Tuning MOFs towards High-Performance Post-Combustion CO_2 Capture Materials. Chem. Commun 2016, 52 (3), 443–452. 10.1039/C5CC07751F.

(78). Yu J; Xie L-H; Li J-R; Ma Y; Seminario JM; Balbuena PB CO_2 Capture and Separations Using MOFs: Computational and Experimental Studies. Chem. Rev 2017, 117 (14), 9674–9754. 10.1021/acs.chemrev.6b00626. [PubMed: 28394578]

(79). Alkhabbaz MA; Bollini P; Foo GS; Sievers C; Jones CW Important Roles of Enthalpic and Entropic Contributions to CO_2 Capture from Simulated Flue Gas and Ambient Air Using Mesoporous Silica Grafted Amines. J. Am. Chem. Soc 2014, 136 (38), 13170–13173. 10.1021/ja507655x. [PubMed: 25215519]

(80). Xu X; Song C; Andresen JM; Miller BG; Scaroni AW Novel Polyethylenimine-Modified Mesoporous Molecular Sieve of MCM-41 Type as High-Capacity Adsorbent for CO_2 Capture. Energy Fuels 2002, 16 (6), 1463–1469. 10.1021/ef020058u.

(81). Mason JA; McDonald TM; Bae T-H; Bachman JE; Sumida K; Dutton JJ; Kaye SS; Long JR Application of a High-Throughput Analyzer in Evaluating Solid Adsorbents for Post-Combustion Carbon Capture via Multicomponent Adsorption of CO_2, N_2, and H_2O. J. Am. Chem. Soc 2015, 137 (14), 4787–4803. 10.1021/jacs.5b00838. [PubMed: 25844924]

(82). Liao P-Q; Chen X-W; Liu S-Y; Li X-Y; Xu Y-T; Tang M; Rui Z; Ji H; Zhang J-P; Chen X-M Putting an Ultrahigh Concentration of Amine Groups into a Metal–Organic Framework for CO_2 Capture at Low Pressures. Chem. Sci 2016, 7 (10), 6528–6533. 10.1039/C6SC00836D. [PubMed: 27928493]

(83). Bien CE; Chen KK; Chien S-C; Reiner BR; Lin L-C; Wade CR; Ho WSW Bioinspired Metal–Organic Framework for Trace CO_2 Capture. J. Am. Chem. Soc 2018, 140 (40), 12662–12666. 10.1021/jacs.8b06109. [PubMed: 30256632]

(84). Darunte L; Sen T; Bhawanani C; Walton KS; Sholl DS; Realff MJ; Jones CW Moving Beyond Adsorption Capacity in Design of Adsorbents for CO_2 Capture from Ultra-Dilute Feeds: Kinetics of CO_2 Adsorption in Materials with Stepped Isotherms. Ind. Eng. Chem. Res 2019, 58 (1), 366–377. 10.1021/acs.iecr.8b05042.

(85). Zhang W; Shan Y; Seidel-Morgenstern A Breakthrough Curves and Elution Profiles of Single Solutes in Case of Adsorption Isotherms with Two Inflection Points. J. Chromatogr. A 2006, 1107 (1–2), 216–225. 10.1016/j.chroma.2005.12.094. [PubMed: 16442120]

(86). Helfferich FG; Carr PW Non-Linear Waves in Chromatography. J. Chromatogr. A 1993, 629 (2), 97–122. 10.1016/0021-9673(93)87026-I.

(87). Golden FM Theory of Fixed-Bed Performance for Ion Exchange Accompanied by Chemical Reaction. Ph.D. Thesis, University of California, Berkeley: United States, 1973.

(88). Satyapal S; Filburn T; Trela J; Strange J Performance and Properties of a Solid Amine Sorbent for Carbon Dioxide Removal in Space Life Support Applications. Energy Fuels 2001, 15 (2), 250–255. 10.1021/ef0002391.

(89). Huang HY; Yang RT; Chinn D; Munson CL Amine-Grafted MCM-48 and Silica Xerogel as Superior Sorbents for Acidic Gas Removal from Natural Gas. Ind. Eng. Chem. Res 2003, 42 (12), 2427–2433. 10.1021/ie020440u.

(90). Xu X; Song C; Miller BG; Scaroni AW Influence of Moisture on CO_2 Separation from Gas Mixture by a Nanoporous Adsorbent Based on Polyethylenimine-Modified Molecular Sieve MCM-41. Ind. Eng. Chem. Res 2005, 44 (21), 8113–8119. 10.1021/ie050382n.

(91). Serna-Guerrero R; Belmabkhout Y; Sayari A Further Investigations of CO_2 Capture Using Triamine-Grafted Pore-Expanded Mesoporous Silica. Chem. Eng. J 2010, 158 (3), 513–519. 10.1016/j.cej.2010.01.041.

(92). Serna-Guerrero R; Belmabkhout Y; Sayari A Triamine-Grafted Pore-Expanded Mesoporous Silica for CO_2 Capture: Effect of Moisture and Adsorbent Regeneration Strategies. Adsorption 2010, 16 (6), 567–575. 10.1007/s10450-010-9253-y.

(93). Goeppert A; Czaun M; May RB; Prakash GKS; Olah GA; Narayanan SR Carbon Dioxide Capture from the Air Using a Polyamine Based Regenerable Solid Adsorbent. J. Am. Chem. Soc 2011, 133 (50), 20164–20167. 10.1021/ja2100005. [PubMed: 22103291]

(94). Fan Y; Lively RP; Labreche Y; Rezaei F; Koros WJ; Jones CW Evaluation of CO_2 Adsorption Dynamics of Polymer/Silica Supported Poly(ethylenimine) Hollow Fiber Sorbents in Rapid Temperature Swing Adsorption. Int. J. Greenh. Gas Control 2014, 21, 61–71. 10.1016/j.ijggc.2013.11.021.

(95). Didas SA; Sakwa-Novak MA; Foo GS; Sievers C; Jones CW Effect of Amine Surface Coverage on the Co-Adsorption of CO_2 and Water: Spectral Deconvolution of Adsorbed Species. J. Phys. Chem. Lett 2014, 5 (23), 4194–4200. 10.1021/jz502032c. [PubMed: 26278953]

(96). Hahn MW; Steib M; Jentys A; Lercher JA Mechanism and Kinetics of CO_2 Adsorption on Surface Bonded Amines. J. Phys. Chem. C 2015, 119 (8), 4126–4135. 10.1021/jp512001t.

(97). Wang D; Wang X; Song C Comparative Study of Molecular Basket Sorbents Consisting of Polyallylamine and Polyethylenimine Functionalized SBA-15 for CO_2 Capture from Flue Gas. ChemPhysChem 2017, 18 (22), 3163–3173. 10.1002/cphc.201700828. [PubMed: 28940634]

(98). Zhang H; Goeppert A; Olah GA; Prakash GKS Remarkable Effect of Moisture on the CO_2 Adsorption of Nano-Silica Supported Linear and Branched Polyethylenimine. J. CO_2 Util. 2017, 19, 91–99. 10.1016/j.jcou.2017.03.008.

(99). Zhao P; Zhang G; Sun Y; Xu Y CO_2 Adsorption Behavior and Kinetics on Amine-Functionalized Composites Silica with Trimodal Nanoporous Structure. Energy Fuels 2017, 31 (11), 12508–12520. 10.1021/acs.energyfuels.7b02292.

(100). Leal O; Bolívar C; Ovalles C; García JJ; Espidel Y Reversible Adsorption of Carbon Dioxide on Amine Surface-Bonded Silica Gel. Inorganica Chim. Acta 1995, 240 (1), 183–189. 10.1016/0020-1693(95)04534-1.

(101). Chang ACC; Chuang SSC; Gray M; Soong Y In-Situ Infrared Study of CO_2 Adsorption on SBA-15 Grafted with γ-(Aminopropyl)Triethoxysilane. Energy Fuels 2003, 17 (2), 468–473. 10.1021/ef020176h.

(102). Khatri RA; Chuang SSC; Soong Y; Gray M Carbon Dioxide Capture by Diamine-Grafted SBA-15: A Combined Fourier Transform Infrared and Mass Spectrometry Study. Ind. Eng. Chem. Res 2005, 44 (10), 3702–3708. 10.1021/ie048997s.

(103). Moore JK; Sakwa-Novak MA; Chaikittisilp W; Mehta AK; Conradi MS; Jones CW; Hayes SE Characterization of a Mixture of CO_2 Adsorption Products in Hyperbranched Aminosilica Adsorbents by ^{13}C Solid-State NMR. Environ. Sci. Technol 2015, 49 (22), 13684–13691. 10.1021/acs.est.5b02930. [PubMed: 26477882]

(104). Lee JJ; Chen C-H; Shimon D; Hayes SE; Sievers C; Jones CW Effect of Humidity on the CO_2 Adsorption of Tertiary Amine Grafted SBA-15. J. Phys. Chem. C 2017, 121 (42), 23480–23487. 10.1021/acs.jpcc.7b07930.

(105). Yu J; Chuang SSC The Role of Water in CO_2 Capture by Amine. Ind. Eng. Chem. Res 2017, 56 (21), 6337–6347. 10.1021/acs.iecr.7b00715.

(106). Chen C-H; Shimon D; Lee JJ; Didas SA; Mehta AK; Sievers C; Jones CW; Hayes SE Spectroscopic Characterization of Adsorbed [13]CO_2 on 3-Aminopropylsilyl-Modified SBA15 Mesoporous Silica. Environ. Sci. Technol 2017, 51 (11), 6553–6559. 10.1021/acs.est.6b06605. [PubMed: 28460168]

(107). Yu J; Zhai Y; Chuang SSC Water-Enhancement in CO_2 Capture by Amines: An Insight into CO_2-H_2O Interactions on Amine Films and Sorbents. Ind. Eng. Chem. Res 2018, 57 (11), 4052–4062. 10.1021/acs.iecr.7b05114.

(108). Chen C-H; Shimon D; Lee JJ; Mentink-Vigier F; Hung I; Sievers C; Jones CW; Hayes SE The "Missing" Bicarbonate in CO_2 Chemisorption Reactions on Solid Amine Sorbents. J. Am. Chem. Soc 2018, 140 (28), 8648–8651. 10.1021/jacs.8b04520. [PubMed: 29947515]

(109). Bacsik Z; Ahlsten N; Ziadi A; Zhao G; Garcia-Bennett AE; Martín-Matute B; Hedin N Mechanisms and Kinetics for Sorption of CO_2 on Bicontinuous Mesoporous Silica Modified

with n-Propylamine. Langmuir 2011, 27 (17), 11118–11128. 10.1021/la202033p. [PubMed: 21774480]

(110). Danon A; Stair PC; Weitz E FTIR Study of CO_2 Adsorption on Amine-Grafted SBA-15: Elucidation of Adsorbed Species. J. Phys. Chem. C 2011, 115 (23), 11540–11549. 10.1021/jp200914v.

(111). Aziz B; Hedin N; Bacsik Z Quantification of Chemisorption and Physisorption of Carbon Dioxide on Porous Silica Modified by Propylamines: Effect of Amine Density. Microporous Mesoporous Mater. 2012, 159, 42–49. 10.1016/j.micromeso.2012.04.007.

(112). Mafra L;   endak T; Schneider S; Wiper PV; Pires J; Gomes JRB; Pinto ML Structure of Chemisorbed CO_2 Species in Amine-Functionalized Mesoporous Silicas Studied by Solid-State NMR and Computer Modeling. J. Am. Chem. Soc 2017, 139 (1), 389–408. 10.1021/jacs.6b11081. [PubMed: 27951638]

(113). Serna-Guerrero R; Da'na E; Sayari A New Insights into the Interactions of CO_2 with Amine-Functionalized Silica. Ind. Eng. Chem. Res 2008, 47 (23), 9406–9412. 10.1021/ie801186g.

(114). Yu J; Chuang SSC The Structure of Adsorbed Species on Immobilized Amines in CO_2 Capture: An in Situ IR Study. Energy Fuels 2016, 30 (9), 7579–7587. 10.1021/acs.energyfuels.6b01423.

(115). Lee J-H; Siegelman RL; Maserati L; Rangel T; Helms BA; Long JR; Neaton JB Enhancement of CO_2 Binding and Mechanical Properties upon Diamine Functionalization of M_2(dobpdc) Metal–Organic Frameworks. Chem. Sci 2018, 9 (23), 5197–5206. 10.1039/C7SC05217K. [PubMed: 29997874]

(116). Martell JD; Porter-Zasada LB; Forse AC; Siegelman RL; Gonzalez MI; Oktawiec J; Run evski T; Xu J; Srebro-Hooper M; Milner PJ; Colwell KA; Autschbach J; Reimer JA; Long JR Enantioselective Recognition of Ammonium Carbamates in a Chiral Metal–Organic Framework. J. Am. Chem. Soc 2017, 139 (44), 16000–16012. 10.1021/jacs.7b09983. [PubMed: 28991466]

(117). Bollini P; Choi S; Drese JH; Jones CW Oxidative Degradation of Aminosilica Adsorbents Relevant to Postcombustion CO_2 Capture. Energy Fuels 2011, 25 (5), 2416–2425. 10.1021/ef200140z.
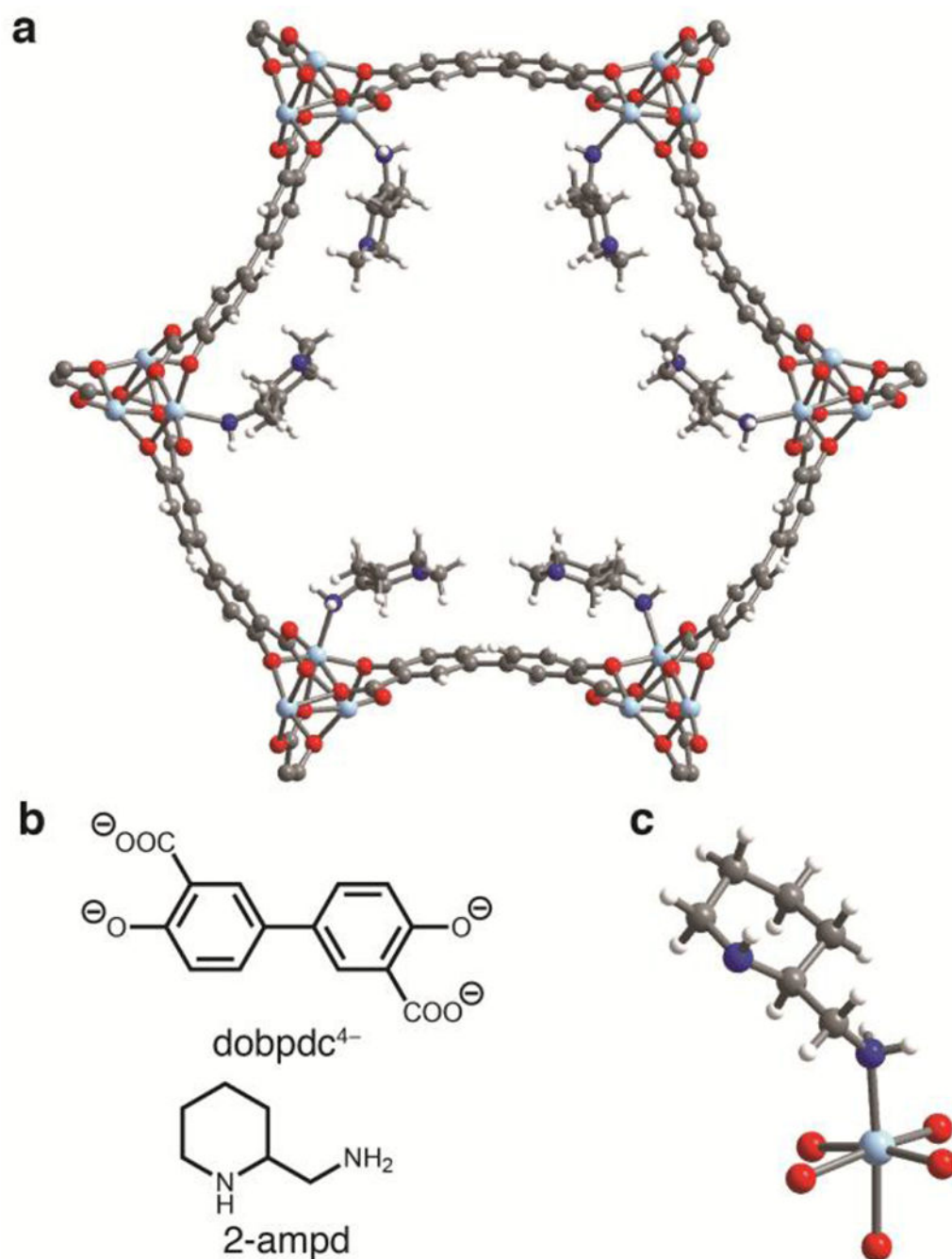
Figure 1.
(a) Single-crystal X-ray diffraction structure of toluene-solvated 2-ampd–Zn$_2$(dobpdc), which is isostructural to 2-ampd–Mg$_2$(dobpdc). The left-handed diamine is depicted in the right-handed framework (space group $P3_121$). The structure was refined with a racemic mixture of 2-ampd in an inversion-twinned crystal. The enantiomeric diamine and toluene solvent molecules are omitted for clarity. (b) Chemical structures of the ligand dobpdc^{4-} and the diamine 2-ampd. (c) First coordination sphere of the Zn(II) site depicting coordination of the left-handed enantiomer of 2-ampd. The diamines were found to coordinate exclusively

through the primary amine. Light blue, blue, red, gray, and white spheres represent Zn, N, O, C, and H atoms, respectively.
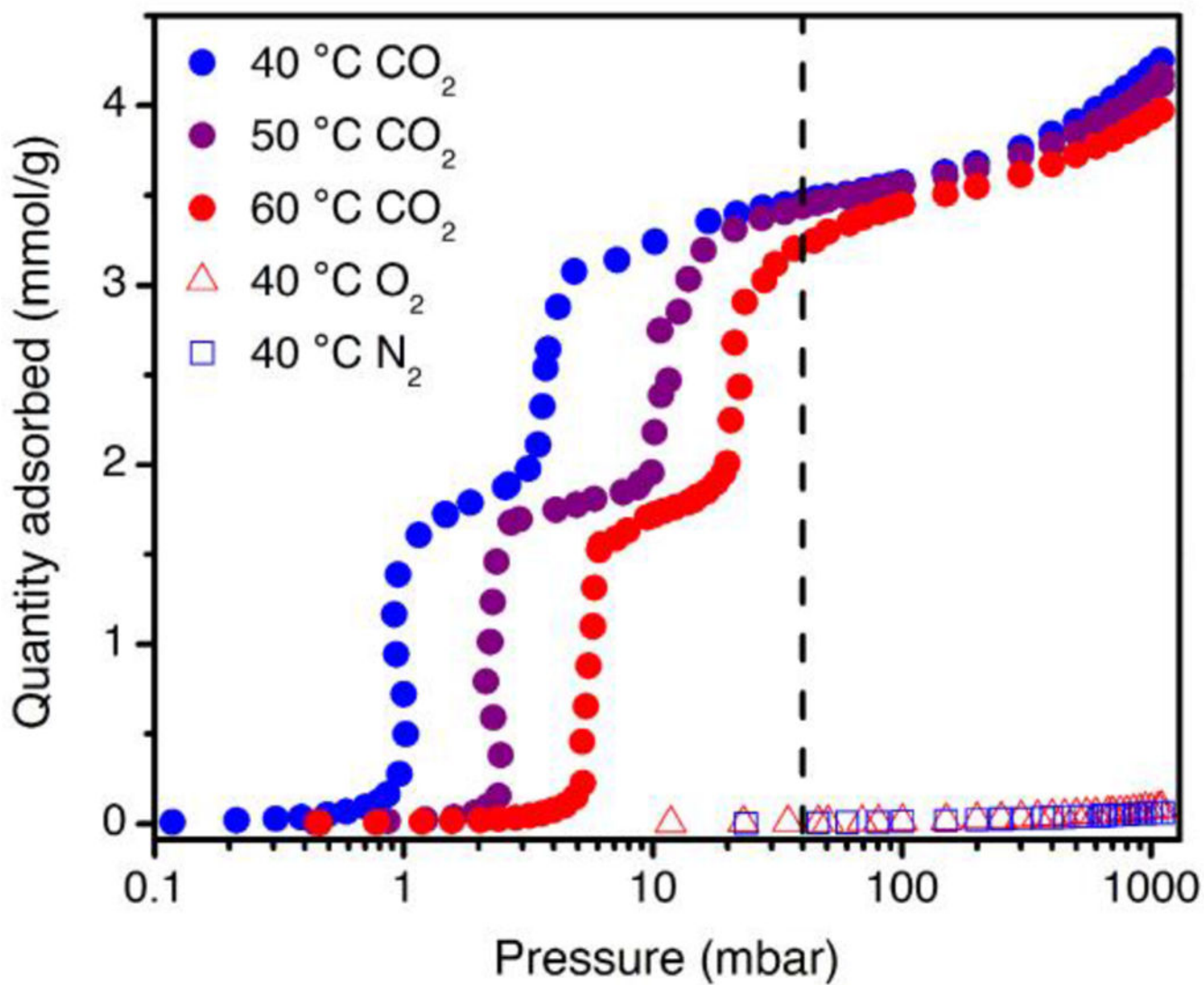
Figure 2.
Pure CO_2 adsorption isotherms at 40, 50, and 60 °C (purple, blue, and red circles, respectively), and for O_2 (red triangles) and N_2 (blue squares) at 40 °C, for 2-ampd–Mg_2(dobpdc). The dashed black line indicates the approximate partial pressure of CO_2 in flue gas from a NGCC power plant (40 mbar).
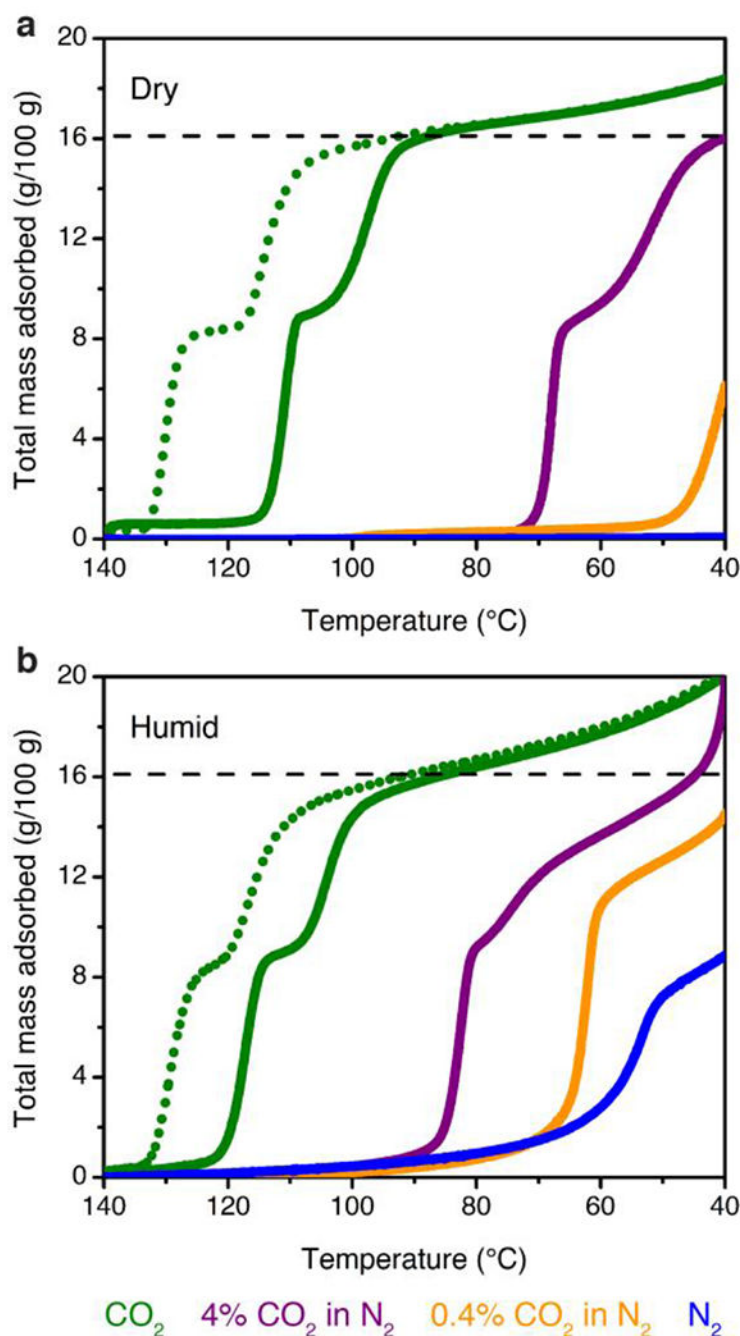
Figure 3.
Dry (a) and humid (b, ~2.6% H_2O) isobars at atmospheric pressure for pure CO_2 (green), 4% CO_2 in N_2 (purple), 0.4% CO_2 in N_2 (orange), and pure N_2 (blue) in 2-ampd–Mg_2(dobpdc). Solid lines depict adsorption (cooling), and dotted green lines depict desorption (heating) for the pure CO_2 isobars. The dashed black lines indicate the theoretical capacity for adsorption of 1 CO_2 per diamine. Temperature ramp rates: 0.5 °C/min for pure CO_2, 0.1 °C/min for 4% and 0.4% CO_2 in N_2, and 1 °C/min for pure N_2.
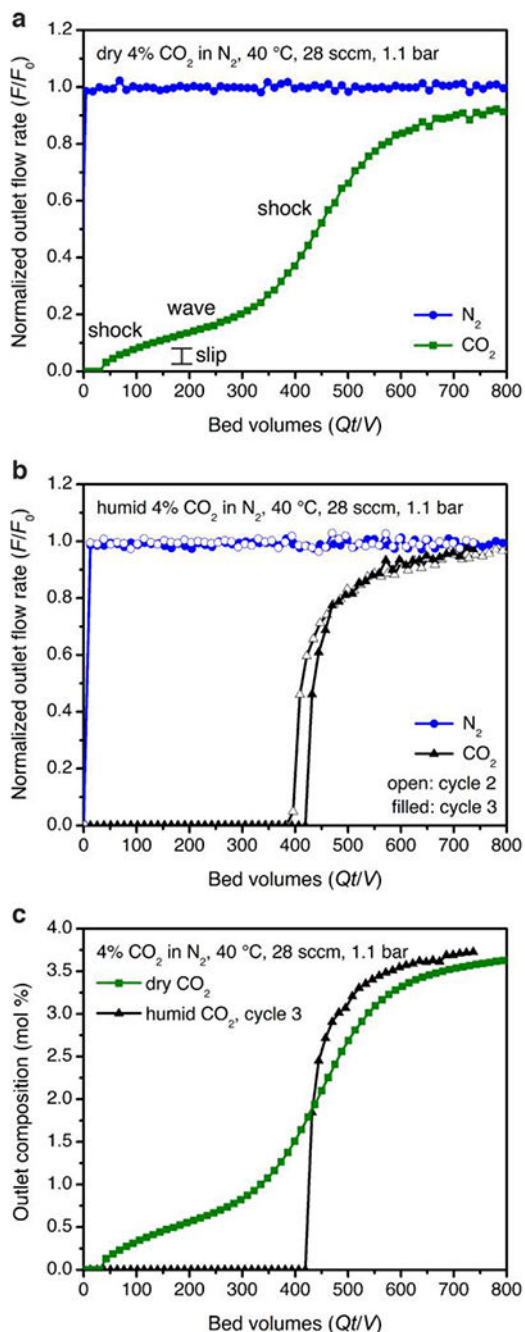
Figure 4.
Breakthrough experiments with 2-ampd–Mg_2(dobpdc) under 28 sccm of a simulated NGCC flue emission stream of 4% CO_2 in N_2 at 40 °C and ~1.1 bar. (a) Experiment with dry simulated flue gas. Capture rate: 86%; exhaustion capacity: 2.4 ± 0.2 mmol/g. (b) Second (filled symbols) and third (open symbols) breakthrough experiment cycles with humid flue gas following pre-saturation of the adsorbent bed with water. Capture rate: >99%; usable capacity (average 90% capture): 2.2 and 2.3 ± 0.1 mmol/g; exhaustion capacity: 2.4 and 2.5 ± 0.1 mmol/g for 2nd and 3rd cycles, respectively. (c) Overlay of dry and humid (3rd cycle)

CO_2 breakthrough profiles. The y-axis is shown as normalized outlet flow rate (F/F_0) in (a) and (b) and as outlet composition in mol % in (c).
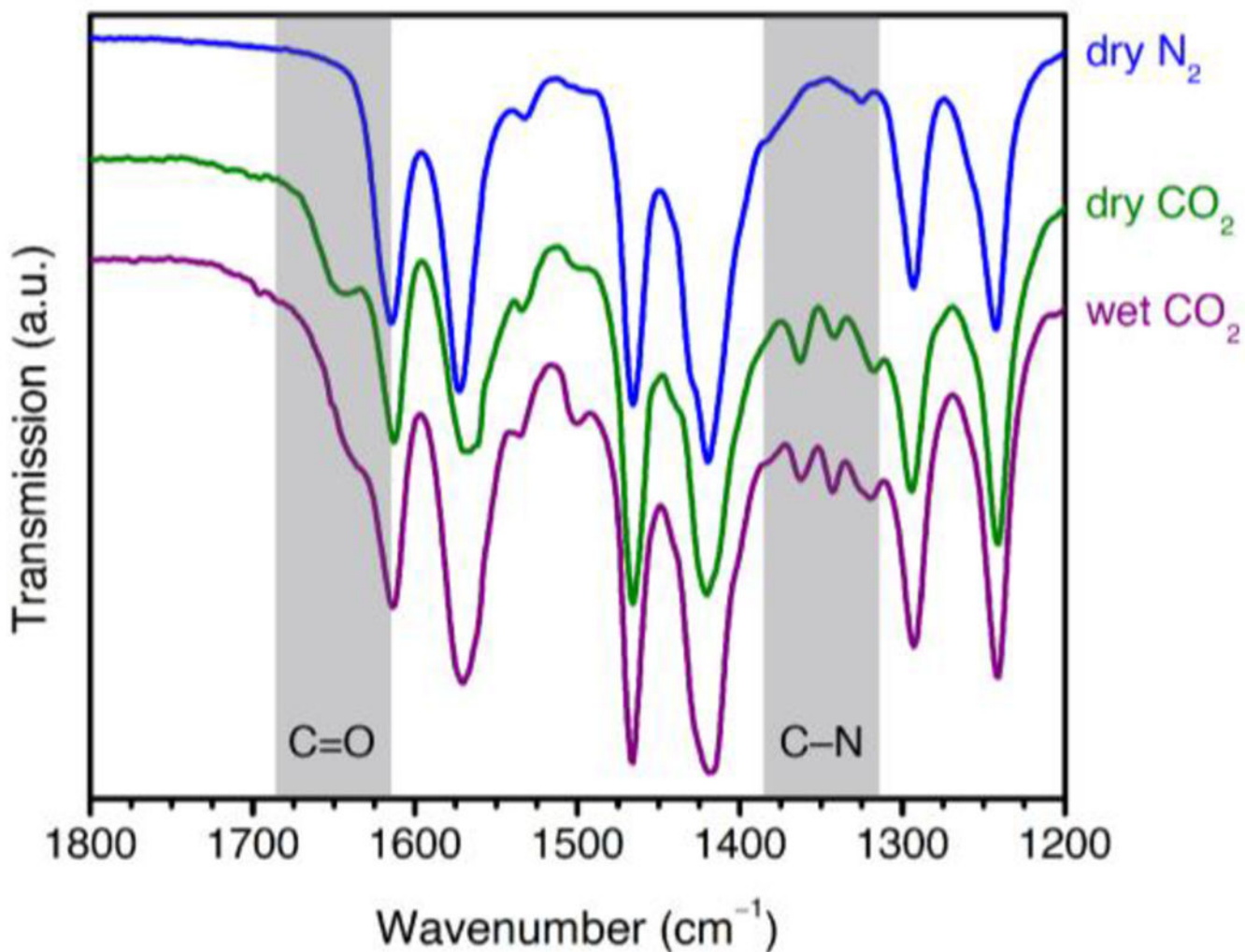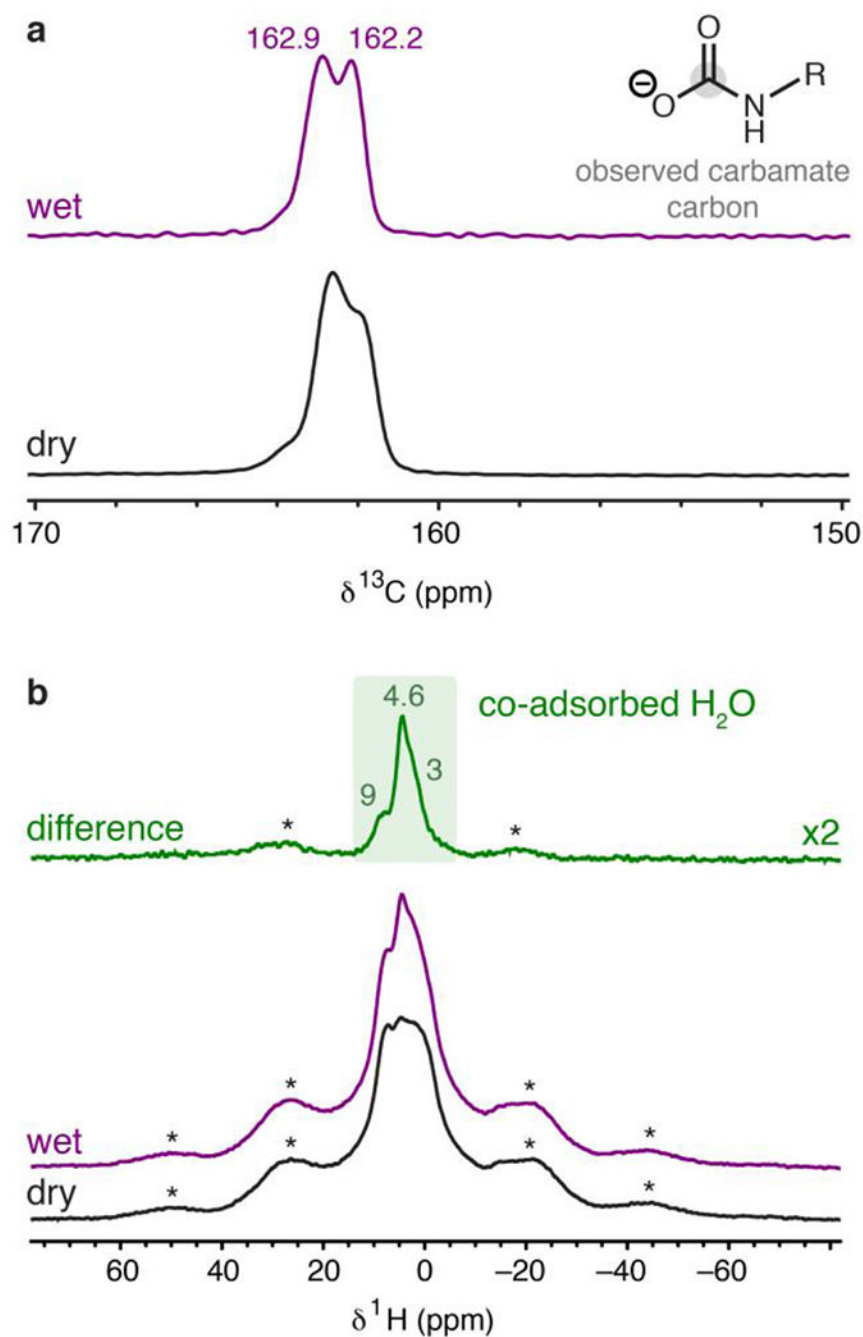
Figure 5.
Infrared spectra of 2-ampd–Mg_2(dobpdc) under dry N_2 (blue), dry CO_2 (green), and humid CO_2 (purple) at room temperature (~22 °C) and atmospheric pressure. The $C(O)O^-$ vibration at 1648 cm^{-1} and C–N//N–$C(O)O^-$ vibrations at 1362 and 1342 cm^{-1} are consistent with the proposed mechanism of ammonium carbamate chain formation under both dry and humid conditions.

Figure 6.
(a) ^{13}C NMR (16.4 T) MAS spectra of 2-ampd–Mg$_2$(dobpdc) dosed with 1025 mbar of dry $^{13}CO_2$ at 22 °C (bottom), and the same sample under a subsequent flow of humid, natural isotopic abundance CO$_2$ at atmospheric pressure (top). Spectra were obtained by cross-polarization from ^{1}H (contact time = 1 ms). Peaks corresponding to the framework linker are not observed due to the low natural abundance of ^{13}C nuclei in the framework compared to the 99% ^{13}C enrichment level for the chemisorbed CO$_2$. (b) ^{1}H NMR spectra obtained by
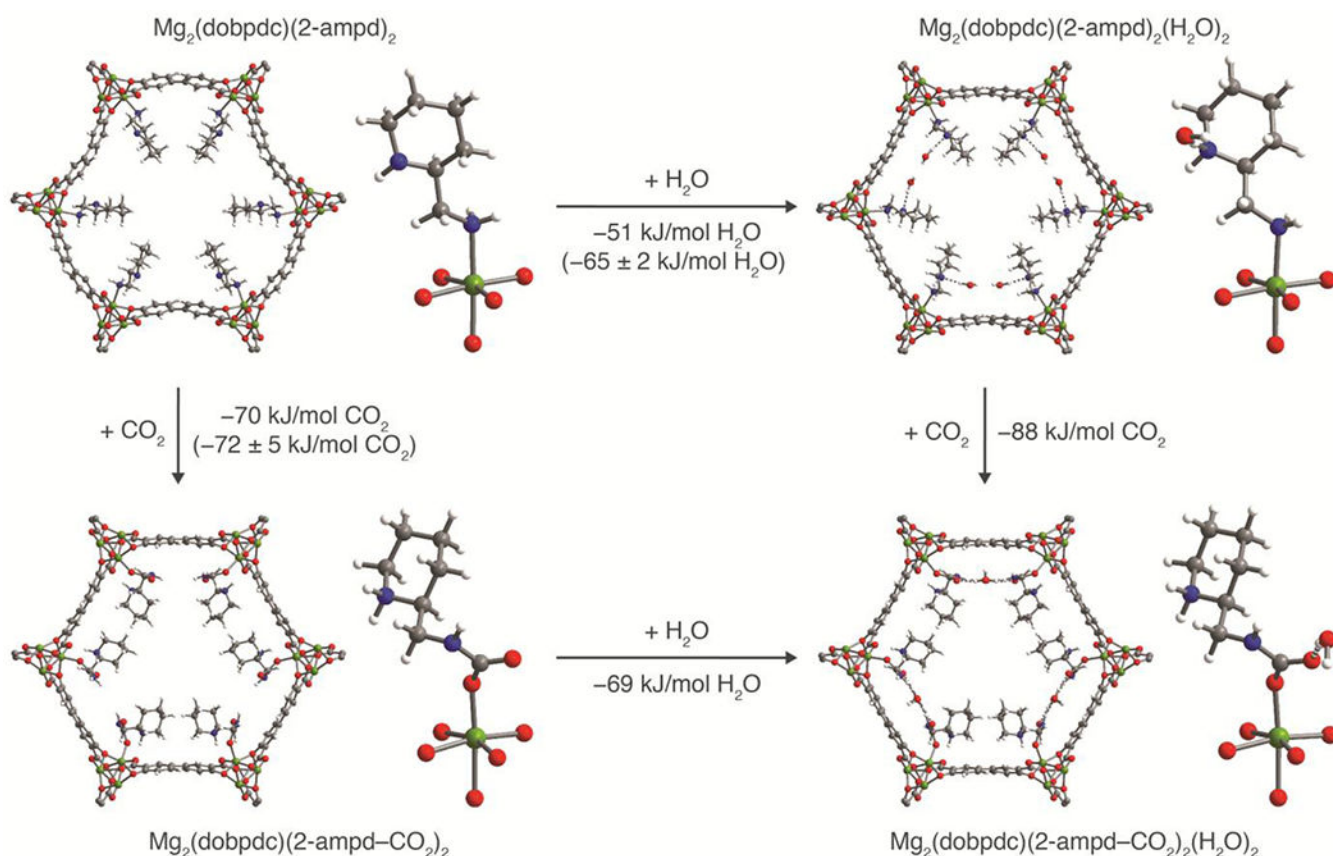
single-pulse excitation for the same samples as in (a). The MAS rate was 15 kHz in all cases. Asterisks mark spinning sidebands.
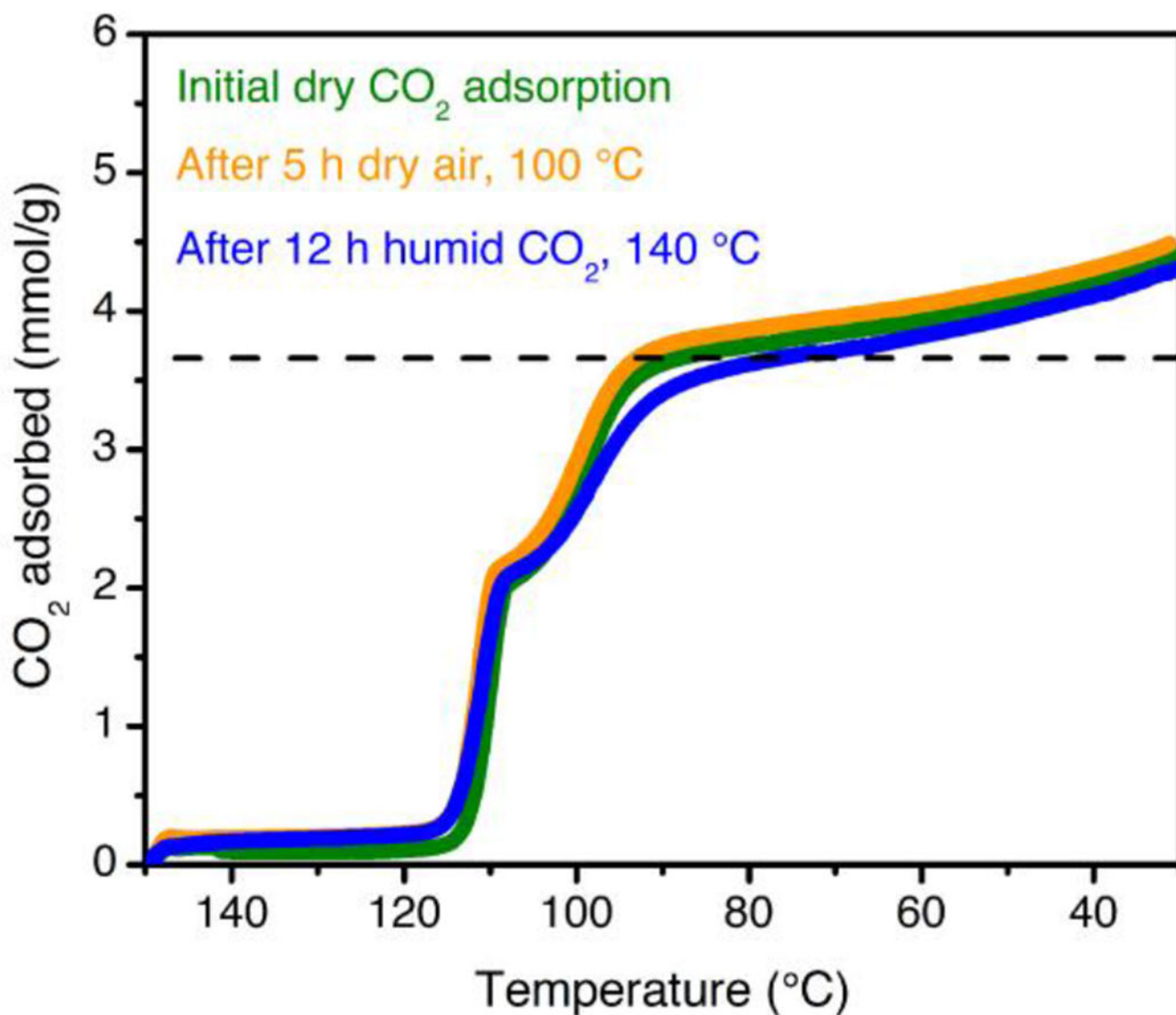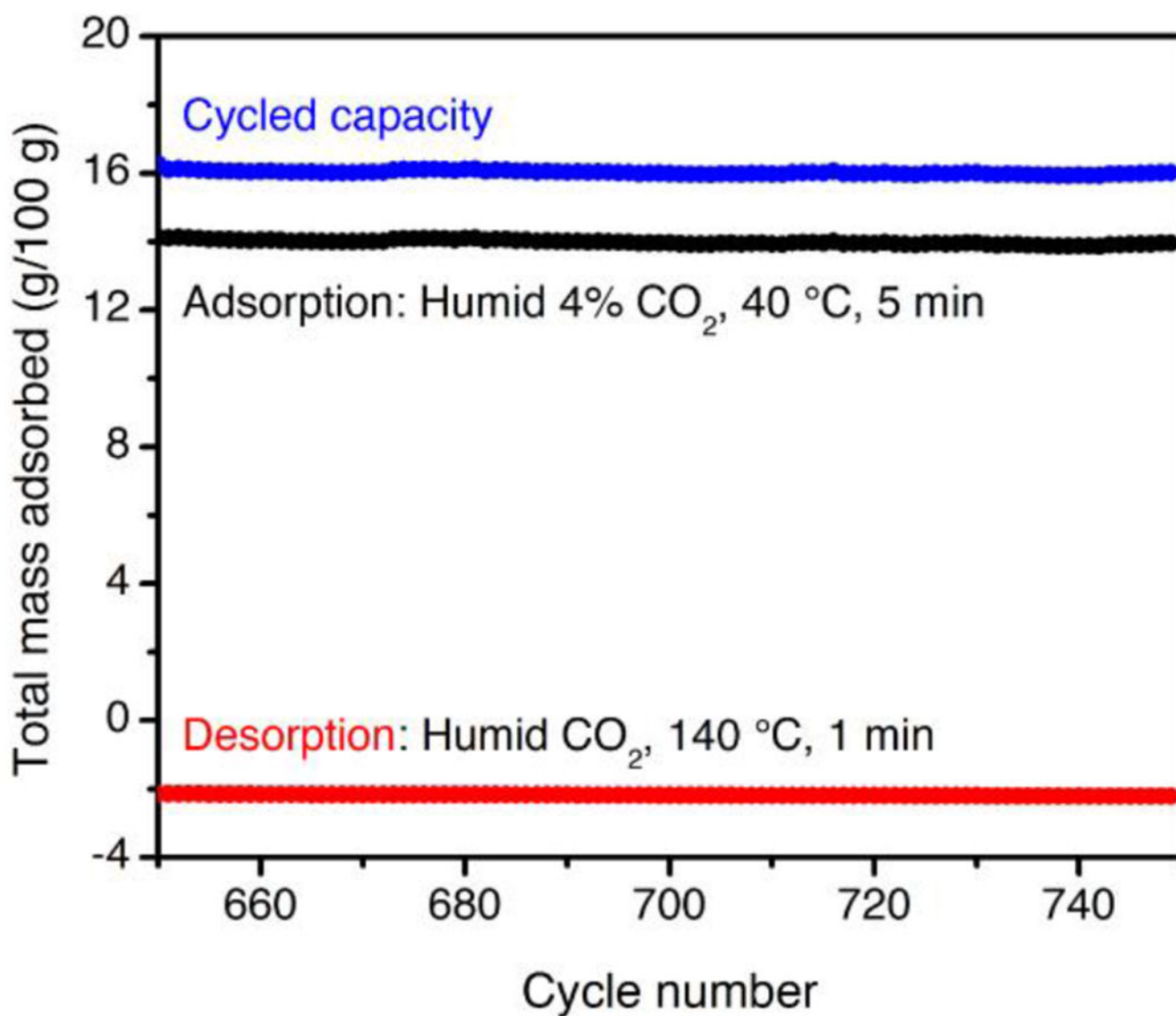
Figure 7.
Projections along the pore axis and first coordination spheres of Mg(II) sites for the vdW-corrected, DFT-calculated structures of evacuated L-2-ampd–R-Mg$_2$(dobpdc) (top left) and the framework following CO$_2$ insertion (bottom left), water adsorption (top right), and co-adsorption of CO$_2$ and H$_2$O (bottom right). The vdW-corrected, DFT-calculated binding energies (E) are provided for each adsorption process, and available experimental differential binding enthalpies (h_{ads}) are included in parentheses. Co-adsorption of water was found to enhance the CO$_2$ binding energy by −18 kJ/mol, and a combined binding energy of −139 kJ/mol 2-ampd was calculated for co-adsorption of 1 CO$_2$ and 1 H$_2$O per diamine. Green, blue, gray, red, and white spheres represent Mg, N, C, O, and H atoms, respectively.

Figure 8.
Dry, pure CO_2 adsorption isobars for 2-ampd–Mg_2(dobpdc) as synthesized (green curve), after exposure to a flow of dry air (~21% O_2 in N_2) at 100 °C for 5 h (orange curve), and after exposure to a flow of humid CO_2 at 140 °C for 12 h (blue curve). A ramp rate of 1 °C/min was used in all cases. The dashed black line indicates the theoretical capacity for adsorption of 1 CO_2 per diamine.

Figure 9.
Cycling data for the final 100 of 750 adsorption/desorption cycles for 2-ampd–Mg_2(dobpdc) in a simulated temperature swing adsorption process. Adsorption: humid 4% CO_2 in N_2, 40 °C, 5 min (black, cycle maxima). Desorption: Humid CO_2, 140 °C, 1 min (red, cycle minima). The cycled capacity (difference) is shown in blue. The baseline value of 0 g/100 g is defined as the mass after activation under 4% CO_2 in N_2 at 150 °C for 20 min prior to the first cycle. The diamine loading was reduced from 100% to 94% after this experiment. The same final loading was observed after 200 adsorption/desorption cycles, suggesting that the diamine loading stabilizes after initial loss. The weight loss due to diamine volatilization correlates with equilibration of the mass upon desorption to the observed negative baseline value.